Bulletin of Volcanology

Electrical resistivity tomography imaging of the near-surface structure of the Solfatara crater, Campi Flegrei (Naples, Italy)
--Manuscript Draft--

Manuscript Number:	BUVO-D-14-00099R4
Full Title:	Electrical resistivity tomography imaging of the near-surface structure of the Solfatara crater, Campi Flegrei (Naples, Italy)
Article Type:	Research Article
Corresponding Author:	Maria Giulia Di Giuseppe, Ph.D. INGV Naples, ITALY
Corresponding Author Secondary Information:	
Order of Authors:	Maria Giulia Di Giuseppe, Ph.D.
	Antonio Troiano, Ph.D.
	Alessandro Fedele, Ph.D.
	Teresa Caputo, Ph.D.
	Domenico Patella, Prof.
	Claudia Troise, Prof.
	Giuseppe De Natale, Prof.
Abstract:	We describe the results from an electrical resistivity tomography (ERT) survey performed inside the Solfatara crater, located in the central part of the Campi Flegrei (CF) composite caldera. The Solfatara volcano represents the most active zone within the CF area, in terms of hydrothermal manifestations and local seismicity. Eight dipole-dipole ERT lines have been measured with the aim of deducting a 3D resistivity model beneath the Solfatara, within the first 80 m depth. The results have allowed a zoning of the shallow structure below the crater in a low-resistivity (LR) class, up to about 4 Ωm, an intermediate resistivity (IR) class, from 5 Ωm up to 50 Ωm, and a high-resistivity (HR) class, from 60 Ωm onward. In order to solve the ambiguities arising in the interpretation of the nature of these bodies, a comparison has been done between the 3D ERT model and the CO_2 flux, soil temperature and gravity maps over the same area. By combining all of these parameters, the whole LR body has been ascribed to a water-dominated geothermal basin and the HR body to a steam/gas-dominated reservoir. Finally, the IR class has been interpreted as a widespread background situation with intermediate character, where volatiles and condensates can coexist in the same volumes with variable percentages, coherently with the resistivity variation within this class. Since fluid dynamics in the Solfatara crater is a rapidly changing phenomenology, ERT surveys repeated in the future are expected to greatly help monitor possible pre-eruptive scenarios, as well as to better follow the local geothermal evolution.
Response to Reviewers:	Dear Editor, we have accepted your edits and we have replied to your comments either changing the text and adding our comments. Thanks and best regards the authors

1 **Electrical resistivity tomography imaging of the near-surface**
2 **structure of the Solfatara crater, Campi Flegrei (Naples,**
3 **Italy)**

4 M.G. Di Giuseppe[1*], A. Troiano[1], A. Fedele[1], T. Caputo[1], D. Patella[2], C. Troise[1], G.
5 De Natale[1]

6 [1] Istituto Nazionale di Geofisica e Vulcanologia (INGV), Osservatorio Vesuviano, Naples,
7 Italy.
8 [2] Department of Physics, University Federico II, Naples, Italy.
9 [*] Corresponding author e-mail: mariagiulia.digiuseppe@ov.ingv.it

10 **Abstract**

11 We describe the results from an electrical resistivity tomography (ERT) survey performed
12 inside the Solfatara crater, located in the central part of the Campi Flegrei (CF) composite
13 caldera. The Solfatara volcano represents the most active zone within the CF area, in terms of
14 hydrothermal manifestations and local seismicity. Eight dipole-dipole ERT lines have been
15 measured with the aim of deducing a 3D resistivity model for the upper 80 m beneath the
16 Solfatara. The results have allowed classification of the shallow structure below the crater into
17 a low-resistivity (LR) class, up to about 4 Ωm, an intermediate resistivity (IR) class, from 5
18 Ωm up to 50 Ωm, and a high-resistivity (HR) class, from 60 Ωm onward. In order to solve the
19 ambiguities arising in the interpretation of the nature of these bodies, a comparison has been
20 done between the 3D ERT model and the CO_2 flux, soil temperature and gravity maps over the
21 same area. By combining all of these parameters, the whole LR body has been ascribed to a
22 water-dominated geothermal basin and the HR body to a steam/gas-dominated reservoir.
23 Finally, the IR class has been interpreted as a widespread background situation with
24 intermediate character, where volatiles and condensates can coexist in the same volumes at
25 variable percentages, coherently with the resistivity variation within this class. Since fluid
26 dynamics in the Solfatara crater change rapidly, ERT surveys repeated in the future are
27 expected to be of great help in monitoring possible pre-eruptive changes, as well as in better
28 following evolution of the local geothermal system.

29 **Keywords**: Campi Flegrei, Solfatara crater, near-surface structure, 3D resistivity tomography

30 **Introduction**

31 The Campi Flegrei (CF) caldera (Fig.1) was formed by huge eruptions 39000 and

32 15000 years ago (Rosi and Sbrana 1987). Vertical ground movements with rates from

33 centimeters to meters per year characterize the dynamics of this area even during

34 quiescent periods (Dvorak and Mastrolorenzo 1991). Since 1969, the area has been in

35 a new phase of uplift after several centuries of subsidence dating back to 1538, when

36 the last eruption occurred in the area (Di Vito et al. 1987). The most recent episodes of

1 intense ground deformation are the two unrests of 1970-72 and 1982-84, causing a
2 cumulative maximum uplift of over 3.5 m, accompanied by intense seismicity. All of
3 the recent literature on the interpretation of such uplift episodes points out the driving
4 role that fluid dynamics and related phase transformation processes have in the area,
5 especially where hydrothermal manifestations are most evident (e.g. De Natale et al.
6 1991; Chiodini et al. 2003; De Natale et al. 2006; Troiano et al. 2011).

7   The Solfatara crater (fig.1) represents the most active zone within the CF
8 caldera. Its activity has long been considered a direct indicator of the volcanic
9 dynamics taking place in the whole caldera. The crater has in fact been the site of
10 intense hydrothermal activity since Greek times, and currently exhibits impressive
11 degassing manifestations. A direct relationship has always been observed between
12 increases in hydrothermal activity in the Solfatara area and ground uplift in the CF
13 caldera.

14   As is well known, geophysics has a prominent role in volcanology. The
15 geophysical mapping of the Solfatara structure is a crucial step for improving our
16 ability to forecast pre-eruptive scenarios, as well as for estimating its geothermal
17 potential. Electrical and electromagnetic (EM) methods are among the most suitable
18 tools, thanks to the large variability and great diagnostic power of the resistivity
19 parameter in volcano-geothermal areas.

20   Only recently, the Solfatara volcano has begun to be surveyed by geoelectrics
21 (Bruno et al. 2007), controlled source audiomagnetotellurics (CSAMT) and natural
22 source magnetotellurics (MT) (Bruno et al. 2007; Troiano et al. 2014). A summary of
23 these results combined with those from gravity and seismic surveys will be given in
24 the next section. What is essential to stress now is that, while the large-scale structure
25 of the volcano, down to a few kilometers depth, has been fairly well imaged across
26 two CSAMT-MT orthogonal profiles, the shallow subsurface of the crater, down to 60
27 m depth, has been only approximately outlined by a 2D inversion of four electrical
28 resistivity tomography (ERT) lines (Bruno et al. 2007). Thus, in order to construct a
29 3D resistivity model of the Solfatara near-surface hydrothermal system, eight new
30 ERT lines were measured in 2013, distributed over the accessible area of the crater
31 (Fig. 2).

1   In the following sections, after providing a geophysical outline of the Solfatara

2   volcano based on previous investigations, results from the new ERT survey will be

3   presented and discussed.

4   **Geophysical outline of Solfatara**

5   The Solfatara volcano (Fig.1) is located inside the CF caldera, about 2 km ENE of the

6   town of Pozzuoli. It is a tuff cone formed 3700-3900 years ago, which in 1198 AD

7   generated a low-magnitude explosive eruption that ejected tephra over a small area (<1

8   km^2) (Di Vito et al. 1999). The crater is made up of a phreatic-magmatic breccia

9   overlain by a sequence of pyroclastic flow deposits, mostly altered by fumarolic

10   activity. It has a nearly elliptical shape with diameters of 580 m and 770 m, and the

11   highest relief along its rim reaches 199 m asl.

12   The Solfatara crater is located very close to the area of maximum ground uplift

13   and is the most active seismic area. It hosts large and spectacular fumarole vents

14   (Fig.2), with maximum flow temperatures in the range 150-160°C at the *Bocca*

15   *Grande* (BG) and *Bocca Nuova* (BN) fumaroles and about 100°C at *Le Stufe* (LS) and

16   *La Fangaia* (LF) ones (Chiodini et al. 2001). Systematic measurements of the gas

17   fluxes from the soil indicate up to 1500 tons/day of CO_2 emission through the main

18   fault system and temperature up to 95°C far from the fumaroles (Granieri et al. 2010).

19   At the LF area, in the west, and the BN and BG areas in the east (Fig.2), anomalously

20   high CO_2 discharge and high seismic noise have been monitored from 2000 to date.

21   Except for the pioneering gravity survey by Oliveri del Castillo et al (1968), the

22   crater has only recently become the site of detailed geophysical prospecting

23   campaigns. Petrosino et al. (2012) obtained an image of the shallow crustal structure

24   of Solfatara by correlating the local seismic noise with the results of a volcanological

25   and morphostructural survey. They observed a coherent, high degree of heterogeneity

26   in shear wave velocity, reflecting lithological contrasts and the structural setting. Their

27   conclusion was that the volcanic edifice was generated by a complex alternation of

28   constructive and destructive phases from an eruptive vent migrating eastwards,

29   subsequently affected by rainfall ~~atmospheric agents~~ and altered by hydrothermal

30   activity. Letort et al. (2012) inferred the main subsurface features of the Solfatara

31   crater by correlating active and passive seismic data with CO_2 flux and soil

3

Comment [A1]: what does this refer to? Wind doesn't really indicate rainfall.

temperature maps. In particular, they were able to define the properties of a near-surface body, localized near the mud pool area (LF area in Fig.2), associated with the top part of a hydrothermal system plume.

Bruno et al. (2007), integrating near-surface TDEM, ERT and seismic profiles with hydrogeological investigations, approximated the subsoil beneath the crater, down to about 60 m depth bgl, as a two-layer sequence. The top layer with average thickness around 20 m was associated with a dry argillitic alteration zone affected by CO_2 degassing. The underlying zone was inferred to be associated with a hydrothermal aquifer recharged by natural condensates through faulted and/or fractured blocks affected by the expulsion of gas-rich hydrothermal fluid.

The deeper structure below the Solfatara crater has also been investigated by CSAMT and MT data. Bruno et al. (2007) analyzed a set of 6 CSAMT-MT soundings, along a N-S-profile on the western side of the crater, deducing that west of the LF area the hydrothermal aquifer extends down to 300-400 m at least, below the ground surface. Most recently, Troiano et al. (2014) have shown the results from a 3D inversion of a combined CSAMT-MT nearly E-W, 1.2 km long profile in the Solfatara crater and adjacent Pisciarelli area (Fig.1), crossing the CSAMT-MT line by Bruno et al. (2007) west of the LF area (Fig.2). Below the Solfatara crater, Troiano et al. (2014) found a 1-10 Ωm conductive body localized west of the LF area and extending from ground surface down to 300-400 m, which was ascribed to a water-saturated, high-pressure geothermal reservoir, in agreement with the finding by Bruno et al. (2007) for the same area. Bruno et al. (2007) highlighted, near Solfatara's eastern rims, a nearly vertical, 50-90 Ωm resistive plumelike structure escaping at about 2 km depth from the top edge of a presumably horizontal, slightly more resistive platelike body. The plumelike structure reaches the free surface where the BN and BG fumarole fields are active (Fig.2), whereas the platelike structure extends at least down to the 3 km maximum depth of EM exploration. Based on *P*-to-*S* wave velocity ratios, gravity and geochemical data, the plumelike portion has been interpreted as a steam/gas-saturated column and the platelike portion to a high temperature (>300°C), over-pressured, gas-saturated reservoir.

The ERT survey in the Solfatara crater

1   As previously said, the resistivity parameter varies strongly, allowing the great

2   majority of buried structures of volcanological and geothermal interest to be

3   distinguished. The ERT approach can greatly enhance the resolution. It involves

4   acquisition of large datasets, which can now be quickly collected using computer-

5   assisted, multichannel resistivity meters. Refined 2D and 3D inversion codes (e.g.

6   Tripp et al. 1984; Shima 1990; Park and Van 1991; Li and Oldenburg 1992; Sasaki

7   1994; Loke and Barker 1995; Dahlin and Zhou 2004; Mauriello and Patella 2009)

8   further strengthen ERT, making it very effective for imaging volcanic structures down

9   to a few hundred meters depth (e.g. Di Maio et al. 1997; 1998a; Bruno et al. 2007;

10   Legaz et al. 2009; Zeyen et al. 2011; Fikos et al. 2012).

11   Eight ERT profiles have been acquired in the Solfatara crater (Fig.2) using a

12   Dipole-Dipole (DD) electrode configuration with a full array of maximum 72

13   electrodes. In confined areas where it was difficult to manage cable layouts, as in the

14   Solfatara crater, we found it effective to use the DD source-receiver coupling, because

15   it is more compact and is both sensitive to lateral location and facilitates depth

16   evaluation of anomaly source bodies (Ward 1990). For the source we used the IRIS

17   Syscal Pro system with maximum output voltage and current of 800 V and 2 A,

18   respectively. Six 230 m long profiles (ERT1, ERT2, ERT4, ERT5, ERT6 and ERT7)

19   were characterized by a minimum electrode spacing of 5 m and maximum depth of

20   penetration of about 40 m. Two 550 m long profiles (ERT3 and ERT8), each

21   composed of two overlapping segments, were also realized, characterized, instead, by

22   a 10 m minimum electrode spacing and maximum depth of penetration of about 80 m.

23   The apparent resistivity pseudosections across the ERT1, ERT2, ERT4, ERT5,

24   ERT6 and ERT7 profiles are drawn in Fig.3a, those across the ERT3 and ERT8

25   profiles in Fig.3b. Pseudosection plots are obtained by contouring the apparent

26   resistivity values and are a convenient means to display the data, but have only a rough

27   relationship with the real resistivity pattern. Shape and amplitude of the anomalies,

28   which strictly represent shifts among different apparent resistivity values, depend on

29   the unknown true resistivity pattern and data density, and also on contamination due to

30   even small inhomogeneities close to electrodes. We have used the criterion of placing

31   the vertical position of the plotting point at the median depth of investigation, or

32   pseudodepth, of the DD array (Edwards 1977).

1   An inspection of the eight pseudosections reveals, along all of the profile

2 directions, diffuse lateral and vertical heterogeneities within an apparent resistivity

3 range of about 2.5 orders of magnitude. Sometimes, sharply different results are

4 obtained in the same pseudodepth range between nearby profiles. The most striking of

5 such effects is the red spot with apparent resistivity values ranging between 20 Ωm

6 and 100 Ωm, appearing in the distance range 120-160 m and pseudodepth range 20-40

7 m along the ERT5 profile. Nothing similar is evident along the nearby ERT7 profile,

8 where, instead, apparent resistivity values are around 8 Ωm in almost the same

9 inspected volume. Effects like this are not surprising when using the DD electrode

10 array, because this array is very sensitive to electrode effects and invariably produces

11 ERT graphs with a large scatter in the measured points (Van Zijl 1985; Ward 1990).

12   In conclusion, we infer strong 3D inhomogenities in the near-surface structure of

13 the crater. It was thus felt necessary to proceed with a full 3D inversion of all of the

14 ERT profiles. To accomplish this aim, we use the PERTI method (Mauriello and

15 Patella 2009), which is a very fast, user-friendly inversion tool, quite appropriate for

16 dealing with a great multiplicity of data sets collected along even randomly oriented

17 profiles. For the interested reader, an outline of the PERTI theory is given in the

18 appendix.

19 **The 3D resistivity model of the Solfatara crater**

20 We show now the results obtained from the application of the PERTI algorithm to the

21 whole ERT data set, collected along the lines drawn in Fig.2. Six resistivity maps at

22 different depths have been plotted (Fig.4). In all of the maps, the depth is referred to

23 the zero level taken in correspondence with the flat ground surface in the large central

24 area of the crater, at 93 m mean altitude above sea level. We stress that the shallower

25 maps are much better resolved than the deeper ones, thanks to the much greater

26 number of datum points available within the pseudodepth range from ground surface

27 down to 40 m. The deeper maps, in fact, are constrained by a number of datum points

28 that rapidly decreases from 40 m down to 80 m, since this pseudodepth range has been

29 reached only by the two nearly orthogonal profiles ERT3 and ERT8 on gradually

30 shorter segments. A consequence of this is that in all of the points of the two deeper

1 maps at 60 m and 80 m bgl in Fig.4, lacking any measured apparent resistivity values,

2 the PERTI tool has just linearly predicted resistivity.

3   Since this is the first application of the PERTI tool to volcanology, the ideal

4 approach for assessing the confidence level of its results is to compare them with those

5 derived from a standardised program, like the renowned RES3DINV and ERTlab 3D

6 commercial softwares, as was done in some recent applications to archaeology

7 (Cozzolino et al. 2012; 2014). The difficulty, however, is that we could not directly

8 apply any of those programs to the present case, because of the random directions of

9 the profiles. Therefore, we decided to use for comparison the approximate model

10 resulting from the 3D interpolation of the single 2D inversions of the ERT profiles

11 obtained using the RES2DINV program.

12   Fig.5 shows the approximate model thus derived, using the same sequence of

13 maps as for the PERTI model in Fig.4. The comparison between the two models

14 shows an overall structural similarity in terms of the gross geometrical features, as

15 well as the resistivity range that characterizes the whole surveyed area. The main

16 difference is in the shapes of the boundaries of the bodies, which in Fig.5 are

17 considerably affected by spurious dragging effects due to the interpolation process,

18 which creates adjacent bodies with improbably strongly contrasting resistivity. We

19 consider the risk of generating artefacts is higher when using a 3D reconstruction from

20 2D inversions, because interpolation based on 2D inversion models necessarily rubs

21 out details between profiles. We are confident that the PERTI model in Fig.4 provides

22 a reasonable solution to the 3D inversion problem of the Solfatara database.

23   To support this conclusion we illustrate the results from the analysis of the

24 degree of similitude between the field apparent resistivity dataset and the simulated

25 apparent resistivity dataset derived from the PERTI model of Fig.4, using a subroutine

26 of the RES3DINV software apt to solve the direct problem. The degree of similitude

27 has been quantified using the dimensionless discrepancy index, $d(P_i)$, given as

28 $$d(P_i) = \frac{\rho_{a,f}(P_i) - \rho_{a,s}(P_i)}{\rho_{a,s}(P_i)}, \quad i=1,2,...,N, \tag{1}$$

29 where $\rho_{a,f}(P_i)$ and $\rho_{a,s}(P_i)$ are the field apparent resistivity and the simulated apparent

30 resistivity, respectively, both assigned at the same i-th attribution point P_i, and N is the

31 total number of attribution points. It is easy to verify that $d(P_i) \in \,]-1,+\infty[$. Fig.6 shows a

7

1 sequence of maps at increasing pseudodepths, where the modulus of the discrepancy

2 index is contoured. Apart from a negligible number of points (reddish points in Fig.6),

3 where $|d(P_i)|$ is exceedingly high, from 1 up to 1.5, and a few small areas (yellowish

4 areas), where $|d(P_i)|$ varies around 0.6, in all of the slices $|d(P_i)|$ appears clustered in

5 two subsets. In the first subset, which includes all of the greenish areas, $|d(P_i)|$ varies

6 around 0.3, while in the second subset, which includes all of the bluish areas, $|d(P_i)|$

7 ranges between 0 and 0.15.

8   The $d(P_i)$ dataset can be used to estimate the RMS error, defined as (e.g. Feng et

9 al. 2014; Loke 2014)

10 $$\mathrm{RMS} = \sqrt{\frac{\Delta\mathrm{r}^T \Delta\mathrm{r}}{N}}, \tag{2}$$

11 where $\Delta\mathbf{r}$ is the data residual vector, namely, the difference of the N-dimensional

12 vector with components $\log[\rho_{a,f}(P_i)]$ and the N-dimensional vector with components

13 $\log[\rho_{a,s}(P_i)]$, with the superscript T denoting transposition. Using the definition in eq.1,

14 after a few simple mathematical steps, one obtains

15 $$\mathrm{RMS} = \sqrt{\frac{\sum_{i=1}^{N}\{log[1+d(P_i)]\}^2}{N}}. \tag{3}$$

16 By inserting in eq.3 the $d(P_i)$ dataset, whose modulus is plotted in Fig.6, we obtained a

17 percent RMS error of 13.26%. This is a fairly satisfactory result from the very fast

18 one-step PERTI algorithm, if one considers the great logistical difficulties and the

19 highly heterogeneous resistivity distribution within the crater. It must also be stressed

20 that RMS errors of this order of magnitude, and even much greater, are quite often

21 found in 3D resistivity environments, in different research fields, even when using

22 sophisticated, iterative inversions (e.g. Lapenna et al. 2003; Soupios et al. 2005; 2007;

23 Athanasiou et al. 2007; Giocoli et al. 2008; Aizebeokhai et al. 2010; Ortega et al.

24 2010; Richards et al. 2010; Loke 2014; Vargemezis 2014).

25   Turning back to the maps in Fig.4, their overall coherence was considered

26 sufficient to attempt a 3D zoning in terms of resistivity classes. We started with a

27 visual inspection of the maps, taking into account the conceptual model of the area

28 based on volcanological data. Key aspects of this conception are the widespread

8

1   pyroclastic nature of the surface layer, the diffuse degassing <u>throughout</u> the area, and

2   the presence of a large mud pool, on one side, and vigorous fumarole vents on the

3   other side<u>. These features are all developed in</u> an environment of continual changes

4   caused by the uprising of aggressive hydrothermal fluids of deep origin, self-sealing

5   processes and opening of cracks and fractures. In the maps we note a general low-to-

6   medium resistivity context: resistivity reaches values as low as 1 Ωm, on one side, and

7   does not exceed 200 Ωm, on the other side. The larger detected high resistivity body

8   appears, in fact, <u>to effectively coincide</u> with the BN and BG fumarole vents, while the

9   low resistivity volumes appear to surround the LF area.

10   <u>We also rely on previously published results, though only a few are</u> available

11   (e.g. Byrdina et al. 2014; Di Maio et al. 1998b; Bruno et al. 2007; Troiano et al. 2008;

12   Legaz et al. 2009; Xia et al. 2010; Zeyen et al. 2011; Fikos et al. 2012; Wardman et al.

13   2012). <u>The</u> ways used to classify the resistivity ranges are quite similar. In this regard,

14   <u>we note</u> that volcanic environments in different places, even if phenomenologically

15   comparable, <u>would not have had</u> identical evolution <u>and</u> physicochemical

16   <u>development.</u>

17   Based on these facts, the following three different classes have been identified.

18   The first class, referred to as a low resistivity (LR) class, includes bodies with

19   resistivity ≤4 Ωm, corresponding in Fig.4 with the contoured patches from light blue

20   to violet. In the deeper maps, the LR class occupies a large portion of the SW

21   quadrant. Looking at the shallower maps, the LR class includes a fragmented, arcuate

22   sequence of spots around a wide central part of the crater, which corresponds with the

23   mud pool area (LF area in Fig.2). Of this sequence, the segments <u>in the</u> west and north

24   appear of much larger extent, <u>especially</u> at 30 m depth bgl, while the southern branch

25   is made of smaller, separated spots, which clearly appear only in the map at 40 m bgl.

26   The second class, which we call the high resistivity (HR) class, includes all

27   bodies that have resistivity values ≥60 Ωm, corresponding in Fig.4 with the contoured

28   patches from dark orange to deep red. In the three deeper maps we observe that the

29   HR class includes a rather uniform body situated in the southeast quadrant. Proceeding

30   upwards, this body vanishes, but a small HR channel seems to emerge out of it, rising

31   up to near surface, as documented by the red spot appearing at the eastern margin of

32   the SE quadrant of the three shallower maps. <u>It is also interesting that there is</u> a HR

9

1 volume along the northern margin of the area, clearly visible from 30 m bgl upwards.

2 Finally, we note the presence of a cluster of small red spots only in the maps at z=20 m

3 and z=30 m bgl, located in correspondence with the southern border of the mud pool,

4 with resistivity around the lower limit of the HR-class.

5   The third class, which we call the intermediate resistivity (IR) class, includes all

6 bodies that have resistivity values between 5 Ωm and 50 Ωm, corresponding in Fig.4

7 with the contoured areas from deep green to brownish yellow.

8 **Discussion**

9 We now proceed to interpretation of the model depicted in Fig.4. First we show (Fig.

10 7) a 3D perspective view of the link between the CSAMT-MT section inferred by

11 Troiano et al. (2014) along with the PERTI section slice at z=80 m bgl, viewed from

12 the bottom,from the 3D ERT model presented in this paper. The line of intersection of

13 the two cross sections corresponds with the trace of the CSAMT-MT profile, drawn

14 with a cyan dashed line in Fig.2. With respect to the general resistivity pattern, the

15 correspondence along the junction line appears, at a large scale, quite good. Since the

16 average distance between any two contiguous CSAMT station sites along the profile

17 was about 100 m, the uppermost portion of the CSAMT-MT depth section may be

18 looked at as a smoothed version of the ERT resistivity distribution along the junction

19 line. We recall now that the electrically conductive body localised west of the LF area

20 by the CSAMT-MT survey was ascribed by Troiano et al. (2014) to a water-saturated,

21 high-pressure geothermal reservoir. The resistive zone localised below the BG and BN

22 area was, in contrast, associated with a steam/gas-saturated column. Such

23 correspondences can be used as basic guidelines for the interpretation of the PERTI

24 model. Thus, referring to the LR ERT class, the large volume situated in the western

25 sector, and the smaller bodies all around at variable depth (Fig.4), can be ascribed to

26 porous, permeable rocks saturated with highly ionized condensates. For the HR ERT

27 class, the large volume situated in the eastern sector and all of the smaller bodies all

28 around, can instead be ascribed to fractured rocks saturated with volatiles.

29   As with the interpretation of the CSAMT-MT data by Troiano et al. (2014),

30 which they did by combining geochemical data, body wave velocity ratio and mass

Comment [A2]: by (= interpretation by Troian or "of" (if this is your interpretation of their data)

Comment [A3]: by. It's their interpretation.

Comment [A4]: their interpretation, or yours?

1 density contrast, a similar approach can now be used to support the above preliminary

2 PERTI model interpretation. Here we consider the CO_2 flux and soil temperature maps

3 presented in Bruno et al. (2007) and the Bouguer anomaly map of Oliveri del Castillo

4 et al (1968).

5   Fig.8 shows the map of CO_2 flux superimposed on a ~~plan~~ top view of the

6 resistivity isosurfaces of the ~~a synthetic 3D version of the~~ PERTI model. We observe

7 in the central crater area a cluster of closely spaced highs in CO_2 flux. What seems

8 noteworthy is that the higher CO_2 peaks occur within and west of the BN-BG area. In

9 particular, the highest CO_2 peak appears exactly in correspondence with the tube-like

10 HR body arising from the deeper large HR structure in the SE quadrant of the area. In

11 contrast, the less intense CO_2 peaks appear to correspond to those portions of the IR

12 class where, at various depth levels, the resistivity approaches the IR class top limit

13 (see also Fig.4). Fig.8 shows also the map of soil temperature superimposed on the

14 PERTI model ~~plan~~ top view. Since this map looks very similar to that of the CO_2 flux,

15 the correspondence is the same as above. This double comparison seems thus to

16 confirm that within the HR resistivity class there is a general predominance of high

17 temperature volatiles. Condensate fluids should, instead, dominate within the LR

18 bodies, above which no CO_2 and temperature peaks were detected. Lastly, the IR class

19 may reasonably represent intermediate geothermal situations, where both fluid phases

20 coexist and the rock/fluid system evolves to the LR class or the HR class, following

21 the dynamics of the temperature/pressure source field. In detail, predominance of

22 condensates or volatiles is likely to occur where resistivity approaches the bottom or

23 top limit of the IR class, respectively.

24   Finally, Fig.8 shows also the comparison of the Bouguer anomaly map with the

25 PERTI model. Despite the fact that the gravity survey was conducted more than 45

26 years ago, we feel it can give further useful information for the geothermal

27 interpretation of resistivity data.

28   The Bouguer anomaly map of the Solfatara crater is characterized by two gravity

29 lows located in the central area, aligned roughly W-E, each having broadly radial

30 symmetry. The less pronounced minimum to the west spatially correlates quite well

31 with the LR body under the mud pool and surrounding areas. On the other side, the

32 more pronounced minimum appears centered over a large portion of the IR

33 background, where the resistivity approaches the lower limit of the HR class (see

11

Comment [A5]: what is this? density is mass/volume, so this is "mass mass/volume"

Comment [A6]: dimensionality is not clear. either (1) full 3D Perti can be 'collapsed' to a sing 2D plane, or (2) Perti model can be viewed by slic in which case state which slice/plane is viewed. " plan view" implies looking at the uppermost [= 0 mbgl] plane.

Comment [A7]: We show a top view of the 3 isosurfaces of electrical resistivity and we add a the contour of the CO2 flux on the surface.

Comment [A8]: see previous comment. this m be explained earlier, probably back where figure 7 discussed

Fig.4). Only a portion of this gravity minimum correlates with the large volume of HR class material to the east on the PERTI map. To quickly estimate the maximum-depth sources (Bott and Smith 1958; Skeels 1963; Mauriello and Patella 2001) of these two local gravity minima, we have applied Nettleton's formula for spherical bodies, viz. $d=1.305x_{1/2}$ (Nettleton 1971; 1976). In this equation, d is the depth to the center of the source body and $x_{1/2}$ is the half-amplitude width of the anomaly, *i.e.* the horizontal distance from the center of the anomaly to the point where the anomaly is half the value at its center. Referring to Fig.9, where all steps of the approximate interpretation process are depicted, the maximum depths of about 100 m and 75 m bgl have been estimated to be the centers of the west and east source bodies, respectively. Therefore, we interpret the results of the gravity map assuming that its sources are located almost at the same depth ranges as those of the LR body under the mud pool and surrounding areas, on one side, and the large volume of the HR class, on the other side.

For the western, less-pronounced gravity low, qualitatively we can say that the location of its source body appears to correspond with that of the LR volume under the mud pool area. Given that a density decrease is consistent with the expected mass reduction for a rock having an increased proportion of voids, filled with volatiles and/or condensates, the combination of low resistivity and low density in the same body does not contradict the previous conclusion that the LR volume may consist of a hot, highly ionized water-dominated geothermal system.

The adjacent, stronger, gravity low is observed to be located at a depth where its source body could be the HR volume under the BG and BN vigorous fumarole vents. Furthermore, density is expected to be even lower for a steam/gas dominated system than a water-dominated one (Todesco and Berrino 2005). Therefore, if it were not for the horizontal shift eastwards of the bulk HR volume from this gravity low, one could directly say that a lower density combined with a higher resistivity supports the identification of the HR volume under the BG and BN vents as a hot steam/gas-dominated system. To confirm this conclusion, we must admit that such a shift is the result of a migration of the HR volume eastwards during the time between the gravity survey and our survey. We infer that, over the course of the few past decades, some amount of water might, for instance, have invaded spaces previously saturated with steam/gas below the gravity minimum, at the same time as steam/gas fluxes were

1 invading voids opening to the east. It must be stressed in this regard that, east of the

2 crater, close to the outer slopes of the Solfatara volcano, about 600 m far from the BN

3 and BG fumarole vents, the Pisciarelli fumarole field has shown a notable increase of

4 activity since 2003 (Troiano et al. 2014).

5   The only gravity high appearing to north in the map, which to some extent

6 includes the roughly prismatic HR body located a few tens of meters depth below the

7 northern margin of the survey area, represents a concomitant increase in resistivity and

8 density. We ascribe this HR body to a fine-grained, more-compact block of the crater

9 basal breccia, based on the description of volcanic products mapped in the Solfatara

10 (Rosi and Sbrana 1987).

11   Before concluding, we briefly discuss the links between the previous

12 geoelectrical observations by Bruno et al. (2007) and our new ERT results. First, we

13 observe that there is general agreement about the resistivity range describing the near-

14 surface structure of the Solfatara crater, from a few Ωm up to some tens of Ωm.

15 Furthermore, the sequence of slices in Fig.4 shows that the electrical schematization of

16 the crater's subsoil in terms of two layers, hypothesized by Bruno et al. (2007), may be

17 justified from the point of view of the degree of inhomogeneity of the levels. In Fig.4,

18 in fact, the first 30 m of depth bgl appear laterally much more discontinuous than the

19 deeper horizons.

20 **Conclusion**

21 We have described results from an ERT survey performed inside the Solfatara crater,

22 located in the central part of the CF composite caldera, west of Naples, Italy. Eight DD

23 ERT profiles, irregularly aligned due to insurmountable obstacles inside the crater,

24 have been carried out with the aim of producing a 3D resistivity model of deposits in

25 the uppermost 80 m beneath the Solfatara. To this purpose, we have adopted the 3D

26 probability-based ERT inversion (PERTI) method, which has the great advantage of

27 being a very fast inversion tool, quite appropriate for dealing with a great multiplicity

28 of data sets, even when they are collected with randomly distributed profiles. The

29 application to the Solfatara crater has proved the PERTI approach can be used as a fast

30 deconvolution filter also in complex volcano-geothermal environments.

1   The results from the PERTI approach have highlighted a complex resistivity
2   pattern beneath the crater, which we have broken into three resistivity classes, namely
3   a low resistivity (LR) class ($\rho \leq 4$ Ωm), an intermediate resistivity (IR) class (5 Ωm $\leq$
4   $\rho \leq 50$ Ωm) and a high resistivity (HR) class ($\rho \geq 60$ Ωm). Comparison with previous
5   geophysical and geochemical maps of the crater area allows us to ascribe a low density
6   volume of the LR class, localized in the south-western sector of the crater where there
7   is a well-known mud pool (*La Fangaia*) area, to a highly ionized, water-dominated
8   geothermal reservoir. It has also allowed us to attribute a larger, lower density, volume
9   of the HR class, localized in the southeastern sector of the crater among the *Bocca*
10 *Grande* and *Bocca Nuova* main fumarole fields, to a steam/gas-dominated basin.
11 Finally, the IR class has been ascribed to a widespread background environment with
12 intermediate hydrothermal features, where volatiles and condensates can coexist in the
13 same volumes with variable percentages, consistent with the resistivity variations
14 within the class.

15 To conclude, it has been confirmed that resistivity is mostly conditioned by the
16 fluid phases in rocks, an resistivity analysis has the specific ability to distinguish
17 water-dominated from gas-dominated situations. Therefore, because fluid dynamics in
18 active volcano-geothermal areas change rapidly, we think repeated ERT surveys in the
19 Solfatara crater are important in monitoring possibly pre-eruptive resistivity changes,
20 and for better following evolution of the local geothermal system.

21 **Appendix**
22 **Outline of the PERTI method**

23 The 3D PERTI method was proposed by Mauriello and Patella (2009) in the framework of the
24 probability tomography theory, which is now briefly outlined in order to better introduce the
25 basic principle underlying the inversion algorithm.
26   Probability tomography was at first suggested for the self-potential method to identify
27 the places underground, where higher is the occurrence probability of the sources that cause
28 the anomalies detected on the ground (Patella 1997a; 1997b). In geoelectrics, a similar
29 approach was formulated to image the most probable location of the resistivity anomaly
30 source bodies, consisting in plotting the occurrence probability function $\eta\left(P_q\right)$, calculated at a
31 grid of points P_q (q=1,2,…,Q) below the ground surface by the formula (Mauriello and Patella
32 1999)
33 $\eta\left(P_q\right) = C_q \sum_{k=1}^{K} \sum_{j_k=1}^{J_k} \left[\rho_a\left(P_{j_k}\right) - \rho\right] \Psi\left(P_{j_k}, P_q\right).$
34 (A1)
35 In eq.A1, $\rho_a\left(P_{j_k}\right)$ is the measured apparent resistivity at P_{j_k}, *i.e.* the j_k-th nodal datum point of
36 the k-th profile (j_k=1,2,…,J_k; k=1,2,…,K), ρ is the resistivity of a homogeneous, isotropic half-

14

space assumed as reference, or starting model, C_q is a positive-definite non null normalization factor, given by

$$C_q = \left\{ \sum_{k=1}^{K} \sum_{j_k=1}^{J_k} [\rho_a(P_{j_k}) - \rho]^2 \cdot \sum_{k=1}^{K} \sum_{j_k=1}^{J_k} \Psi^2(P_{j_k}, P_q) \right\}^{-1/2}$$

(A2)

and $\Psi(P_{j_k}, P_q)$ is the j_k-th Frechet derivative referred to the reference model, also known as the sensitivity function of the array. It physically describes the effect generated at P_{j_k} by a small perturbation of the reference resistivity at P_q, under Born approximation (Loke and Barker 1995; 1996; Mauriello and Patella 1999).

Including topography, the sensitivity function for the DD array is calculated as follows. Taking a rectangular coordinate system with the *xy*-plane at mean sea level and the *z*-axis upwards, and indicating with $(x_{j_k}^A, y_{j_k}^A, z_{j_k}^A)$, $(x_{j_k}^B, y_{j_k}^B, z_{j_k}^B)$ and $(x_{j_k}^M, y_{j_k}^M, z_{j_k}^M)$, $(x_{j_k}^N, y_{j_k}^N, z_{j_k}^N)$ the coordinates of the current electrodes A and B and potential electrodes M and N, respectively, and with (x_q^P, y_q^P, z_q^P) the coordinates of the model point P_q, $\Psi(P_{j_k}, P_q)$ is explicated asFor (8), the authors may emphasize in the manuscript that the authors interpret the results of gravitational survey assuming that the sources are located almost at same locations although this assumption should be examined.

$$\Psi(P_{j_k}, P_q) = \frac{G_{j_k}}{4\pi^2} \cdot \left(L_{q,j_k}^{AM} - L_{q,j_k}^{AN} - L_{q,j_k}^{BM} + L_{q,j_k}^{BN} \right),$$

(A3)

where G_{j_k} is the geometrical factor of the DD array and

$$L_{q,j_k}^{AM} = \frac{(x_q^P - x_{j_k}^A)(x_q^P - x_{j_k}^M) + (y_q^P - y_{j_k}^A)(y_q^P - y_{j_k}^M) + (z_q^P - z_{j_k}^A)(z_q^P - z_{j_k}^M)}{\left[(x_q^P - x_{j_k}^A)^2 + (y_q^P - y_{j_k}^A)^2 + (z_q^P - z_{j_k}^A)^2 \right]^{3/2} \left[(x_q^P - x_{j_k}^M)^2 + (y_q^P - y_{j_k}^M)^2 + (z_q^P - z_{j_k}^M)^2 \right]^{3/2}}$$

(A4a)

$$L_{q,j_k}^{AN} = \frac{(x_q^P - x_{j_k}^A)(x_q^P - x_{j_k}^N) + (y_q^P - y_{j_k}^A)(y_q^P - y_{j_k}^N) + (z_q^P - z_{j_k}^A)(z_q^P - z_{j_k}^N)}{\left[(x_q^P - x_{j_k}^A)^2 + (y_q^P - y_{j_k}^A)^2 + (z_q^P - z_{j_k}^A)^2 \right]^{3/2} \left[(x_q^P - x_{j_k}^N)^2 + (y_q^P - y_{j_k}^N)^2 + (z_q^P - z_{j_k}^N)^2 \right]^{3/2}}$$

(A4b)

$$L_{q,j_k}^{BM} = \frac{(x_q^P - x_{j_k}^B)(x_q^P - x_{j_k}^M) + (y_q^P - y_{j_k}^B)(y_q^P - y_{j_k}^M) + (z_q^P - z_{j_k}^B)(z_q^P - z_{j_k}^M)}{\left[(x_q^P - x_{j_k}^B)^2 + (y_q^P - y_{j_k}^B)^2 + (z_q^P - z_{j_k}^B)^2 \right]^{3/2} \left[(x_q^P - x_{j_k}^M)^2 + (y_q^P - y_{j_k}^M)^2 + (z_q^P - z_{j_k}^M)^2 \right]^{3/2}}$$

(A4c)

$$L_{q,j_k}^{BN} = \frac{(x_q^P - x_{j_k}^B)(x_q^P - x_{j_k}^N) + (y_q^P - y_{j_k}^B)(y_q^P - y_{j_k}^N) + (z_q^P - z_{j_k}^B)(z_q^P - z_{j_k}^N)}{\left[(x_q^P - x_{j_k}^B)^2 + (y_q^P - y_{j_k}^B)^2 + (z_q^P - z_{j_k}^B)^2 \right]^{3/2} \left[(x_q^P - x_{j_k}^N)^2 + (y_q^P - y_{j_k}^N)^2 + (z_q^P - z_{j_k}^N)^2 \right]^{3/2}}$$

(A4d)

In practice, the average apparent resistivity is assumed as reference uniform resistivity ρ. Hence, $\eta(P_q)$, which is a number between -1 and +1, is interpreted as an occurrence probability measure of a resistivity deviation from ρ at P_q. Positive or negative values of $\eta(P_q)$ give the occurrence probability of an increase or a decrease of resistivity, respectively.

Many field cases were dealt with using this approach, including the Italian volcanic areas of Mt. Etna and Mt. Vesuvius (Mauriello et al. 2004; Mauriello and Patella 2008a; 2008b). In all cases, the mapping of $\eta(P_q)$ proved to be a reliable tool for outlining geometry and location of the source bodies, compatibly with the available data set.

Using eq.A1, no information can, however, be deducted as to the real resistivity values of the structures, geometrically defined by the analysis of the probability index $\eta(P_q)$. Just to find a solution to this last problem that the PERTI method has been proposed. The basic principle for the PERTI method is that the reference resistivity ρ must not be pre-assigned, but assumed to be the unknown true resistivity value ρ_q at P_q. With such an assumption, $\eta(P_q)$ given in eq.A1 can be rewritten as

1 $$\eta(P_q) = C_q \sum_{k=1}^{K} \sum_{j_k=1}^{J_k} [\rho_a(P_{j_k}) - \rho_q] \Psi(P_{j_k}, P_q).$$

2 (A5)

3   The rationale for the PERTI approach is that if $\eta(P_q) = 0$ resulted at P_q, then the most
4 probable resistivity would be there exactly ρ_q. Since it is always $C_q \neq 0$, the $\eta(P_q) = 0$
5 condition allows the following inversion formula to be derived (Mauriello and Patella 2009)

6 $$\rho_q = \frac{\sum_{k=1}^{K} \sum_{j_k=1}^{J_k} \rho_a(P_{j_k}) \Psi(P_{j_k}, P_q)}{\sum_{k=1}^{K} \sum_{j_k=1}^{J_k} \Psi(P_{j_k}, P_q)}.$$ (A6)

7   The most probable real resistivity ρ_q at P_q, compatibly with data accuracy and density
8 and within the assumed first order Born approximation, is simply derived as the weighted
9 average of the apparent resistivity values, using as weights the sensitivity function of the array.
10 Thus, the PERTI formula of eq.A3 can easily be converted into a user-friendly algorithm,
11 quite apt to combine a great multiplicity of large datasets.
12   The main features of the PERTI method, derived from many simulations and field tests
13 (Mauriello and Patella 2009; Cozzolino et al. 2012; 2014), are: (i) independence from a priori
14 information; (ii) absence of iterative processes; (iii) drastic reduction of computing time with
15 respect to standard deterministic inversion tools, like RES3DINV and ERTlab, which may
16 require extremely long time of several hours, compared with the few ten seconds of the PERTI
17 software, to elaborate a set of several thousands data points on a conventional 1 GB RAM PC
18 (Cozzolino et al. 2014); (iv) independence from data acquisition techniques and spatial
19 regularity, unlike the above mentioned commercial softwares, which are designed to invert
20 data collected with a rectangular grid of electrodes.
21   A direct consequence of not requiring a priori information and iterative processes is, for
22 the PERTI method, the uselessness of the computation of the RMS error between measured
23 and modelled apparent resistivity values. The RMS error, whatever is, cannot be lowered in
24 any way within the PERTI theory. Nonetheless, the same tests have shown PERTI modelling
25 results quite comparable with those from the mentioned commercial softwares (Mauriello and
26 Patella 2009; Cozzolino et al. 2012; 2014).

32 **References**

33 Aizebeokhai AP, Olayinka AI, Singh VS (2010) Application of 2D and 3D geoelectrical
34   resistivity imaging for engineering site investigation in a crystalline basement terrain,
35   southwestern Nigeria. Environ Earth Sci 61:1481-1492. doi:10.1007/s12665-010-0464-
36   z

37 Athanasiou EN, Tsourlos PI, Vargemezis GN, Papazachos CB, Tsokas GN (2007) Non-
38   destructive DC resistivity surveying using flat-base electrodes. Near Surface Geophys
39   5:263-272. doi:10.3997/1873-0604.2007008

40 Bott MHP, Smith RA (1958) The estimation of the limiting depth of gravitating bodies.
41   Geophys Prospect 6:1-10. doi:10.1111/j.1365-2478.1958.tb01639.x

42 Bruno PG, Ricciardi GP, Petrillo Z, Di Fiore V, Troiano A, Chiodini G (2007) Geophysical
43   and hydrogeological experiments from a shallow hydrothermal system at Solfatara

Volcano, Campi Flegrei, Italy: Response to caldera unrest. J Geophys Res 112:B06201. doi:10.1029/2006JB004383

Byrdina S, Vandemeulebrouck J, Cardellini C, Legaz A, Camerlynck C, Chiodini G, Lebourg T, Letort J, Motos G, Carrier A, Bascou P (2014) Relations between electrical resistivity, carbon dioxide flux, and self-potential in the shallow hydrothermal system of Solfatara (Phlegrean Fields, Italy). Geophys Res Abs 16. EGU2014-5204.

Chiodini G, Frondini F, Cardellini C, Granieri D, Marini D, Ventura G (2001) CO_2 degassing and energy release at Solfatara volcano, Campi Flegrei, Italy. J Geophys Res 106(B8):16213-16221. doi:10.1029/2001JB000246

Chiodini G, Todesco M, Caliro S, Del Gaudio C, Macedonio G, Russo M (2003) Magma degassing as a trigger of bradyseismic events: The case of Phlegrean Fields (Italy). Geophys Res Lett 30:1434. doi:10.1029/2002GL016790

Chiodini G, Granieri D, Avino R, Caliro S, Costa A, Werner C (2005) Carbon dioxide diffuse degassing and estimation of heat release from volcanic and hydrothermal systems. J Geophys Res 110:B08204. doi:10.1029/2004JB003542

Cozzolino M, Di Giovanni E, Mauriello P, Vanni Desideri A, Patella D (2012) Resistivity tomography in the park of Pratolino at Vaglia (Florence, Italy). Archaeol Prospect 19:253-260. doi:10.1002/arp.1432

Cozzolino M, Mauriello P, Patella D (2014) Resistivity tomography imaging of the substratum of the Bedestan monumental complex at Nicosia, Cyprus. Archaeometry 56:331-350. doi:10.1111/arcm.12018

Dahlin T, Zhou B (2004) A numerical comparison of 2D resistivity imaging with 10 electrode arrays. Geophys Prospect 52:379-398. doi:10.1111/j.1365-2478.2004.00423.x

De Natale G, Pingue F, Allard P, Zollo A (1991) Geophysical and geochemical modeling of the Campi Flegrei caldera. J Volcanol Geoth Res 48:199-222. doi:10.1016/0377-0273(91)90043-Y

De Natale G, Troise C, Pingue F, Mastrolorenzo G, Pappalardo L, Battaglia M, Boschi E (2006) The Campi Flegrei caldera: unrest mechanisms and hazards. In: Troise C, De Natale G, Kilburn CRJ (eds) Mechanics of Activity and Unrest at Large Calderas. Geological Societyof London Special Publications 269, pp 25-45. doi:10.1144/GSL.SP.2006.269.01.03

Di Maio R, Mauriello P, Patella D, Petrillo Z, Piscitelli S, Siniscalchi A, Veneruso M (1997) Self-potential, geoelectric and magnetotelluric studies in Italian active volcanic areas. Ann Geophys 40:519-537. doi:10.4401/ag-3926

Di Maio R, Mauriello P, Patella D, Petrillo Z, Piscitelli S, Siniscalchi A (1998a) Electric and electromagnetic outline of the Mount Somma-Vesuvius structural setting. J Volcanol Geoth Res 82:219-238. doi:10.1016/S0377-0273(97)00066-8

Di Maio R, Gerundo M, Giammetti S, Patella D, Piscitelli S, Veneruso M (1998b) Vulcano: Self-potential mapping and dipolar geoelectric tomography. Acta Vulcanol 10:133-136. ISSN:1121-9114

Di Vito MA, Lirer L, Mastrolorenzo G, Rolandi G (1987) The 1538 Monte Nuovo eruption (Campi Flegrei, Italy). Bull Volcanol 49: 608-615. doi:10.1007/BF01079966

Di Vito MA, Isaia R, Orsi G, Southon J, D'Antonio M, De Vita S, Pappalardo L, Piochi M (1999) Volcanism and deformation since 12,000 years at the Campi Flegrei caldera (Italy). J Volcanol Geoth Res 91:221-246. doi:10.1016/S0377-0273(99)00037-2

Dvorak JJ, Mastrolorenzo G (1991) The mechanisms of recent vertical crustal movements in Campi Flegrei caldera, Southern Italy. GSA Special Papers 263, pp 1-47. doi:10.1130/SPE263-p1

Edwards LS (1977) A modified pseudosection for resistivity and induced-polarization. Geophysics 42:1020-1036. doi:10.1190/1.1440762

Feng D, Dai Q, Xiao B (2014) Contrast between 2D inversion and 3D inversion based on 2D high-density resistivity data. Trans Nonferrous Met Soc China 24:224-232. doi:10.1016/S1003-6326(14)63051-X

Fikos I, Vargemezis G, Zlotnicki J, Puertollano JR, Alanis PB, Pigtain RC, Villacorte EU, Maliport GA, Sasai Y (2012) Electrical resistivity tomography study of Taal volcano hydrothermal system, Philippines. Bull Volcanol 74:1821-1831. doi:10.1007/s00445-012-0638-5

Giocoli A, Magrì C, Vannoli P, Piscitelli S, Rizzo E, Siniscalchi A, Burrato P, Basso C, Di Nocera S (2008) Electrical Resistivity Tomography investigations in the Ufita Valley (Southern Italy). Ann Geophys 51:213-223. doi:10.4401/ag-4443

Granieri D, Avino R, Chiodini G (2010) Carbon dioxide diffuse emission from the soil: ten years of observations at Vesuvio and Campi Flegrei (Pozzuoli), and linkages with volcanic activity. Bull Volcanol 72:103–118. doi:10.1007/s00445-009-0304-8

Lapenna,V, Lorenzo P, Perrone A, Piscitelli S, Sdao F, Rizzo E (2003) High-resolution geoelectrical tomographies in the study of Giarrossa landslide (southern Italy). Bull Eng Geol Env 62:259–268. doi:10.1007/s10064-002-0184-z

Legaz AV, Vandemeulebrouck JR, Revil A, Kemna A, Hurst AW, Reeves R, Papasin R (2009) A case study of resistivity and self-potential signatures of hydrothermal instabilities, Inferno Crater Lake, Waimangu, New Zealand. Geophys Res Lett 36:L12306. doi:10.1029/2009GL037573

Letort J, Roux P, Vandemeulebrouck J, Coutant O, Cros E, Wathelet M, Cardellini C, Avino R (2012) High-resolution shallow seismic tomography of a hydrothermal area: application to the Solfatara, Pozzuoli. Geophys J Int 189:1725-1733. doi:10.1111/j.1365-246X.2012.05451.x

Li Y, Oldenburg DW (1992) Approximate inverse mappings in DC resistivity problems. Geophys J Int 109:343-362. doi:10.1111/j.1365-246X.1992.tb00101.x

Loke MH, Barker RD (1995) Least-squares deconvolution of apparent resistivity pseudosections. Geophysics 60:1682–1690. doi:10.1190/1.1443900

Loke MH, Barker RD (1996) Rapid least-squares inversion of apparent resistivity pseudosections by a quasi-Newton method. Geophys Prospect 44:131-152. doi:10.1111/j.1365-2478.1996.tb00142.x

Loke MH (2014) Tutorial: 2-D and 3-D electrical imaging surveys. Geotomo Softwares, Penang. www.geotomosoft.com

Mauriello P, Patella D (1999) Resistivity anomaly imaging by probability tomography. Geophys Prospect 47:411-429. doi:10.1046/j.1365-2478.1999.00137.x

Mauriello P, Patella D (2001) Localization of maximum-depth gravity anomaly sources by a distribution of equivalent point masses. Geophysics 66:1431-1437. doi:10.1190/1.1487088

Mauriello P, Patella D (2008a) Geoelectrical anomalies imaged by polar and dipolar probability tomography. Prog Electromagnet Res 87:63-88. doi:10.2528/PIER08092201

18

Resistivity tomography of the Solfatara near-surface structure

Mauriello P, Patella D (2008b) Integration of geophysical datasets by a conjoint probability tomography approach. Application to Italian active volcanic areas. Ann Geophys 51:167-180. doi:10.4401/ag-3042

Mauriello P, Patella D (2009) A data-adaptive probability-based fast ERT inversion method. Prog Electromagnet Res 97:275-290. doi:10.2528/PIER09092307

Mauriello P, Patella D, Petrillo Z, Siniscalchi A, Iuliano T, Del Negro C (2004) A geophysical study of the Mount Etna volcanic area. In: Bonaccorso A, Calvari S, Coltelli M, Del Negro C, Falsaperla S (eds) Mt.Etna: Volcano Laboratory. Geophysical Monograph Series 143 AGU, pp 273-291. ISBN:9780875904085

Nettleton LL (1971) Elementary Gravity and Magnetics for Geologists and Seismologists. Monograph Series 1 SEG, Tulsa

Nettleton LL (1976) Gravity and Magnetics in Oil Prospecting. McGraw-Hill, New York. ISBN:9780070463035

Oliveri del Castillo A, Palumbo A, Percolo E (1968) Contributo allo studio della Solfatara di Pozzuoli (Campi Flegrei) mediante osservazione gravimetriche. Annali Osservatorio Vesuviano 22:217-225

Ortega AI, Benito-Calvo A, Porres J, Pérez-González A, Martín Merino,MA (2010) Applying electrical resistivity tomography to the identification of endokarstic geometries in the Pleistocene sites of the Sierra de Atapuerca (Burgos, Spain). Archaeol Prosp 17:233-245. doi:10.1002/arp.392

Park SK, Van G (1991) Inversion of pole-pole data for 3D resistivity structure beneath arrays of electrodes. Geophysics 56:951-960. doi:10.1190/1.1443128

Patella D (1997a) Introduction to ground surface self-potential tomography. Geophys Prospect 45:653-681. doi:10.1046/j.1365-2478.1997.430277.x

Patella D (1997b) Self-potential global tomography including topographic effects. Geophys Prospect 45:843-863. doi:10.1046/j.1365-2478.1997.570296.x

Petrosino S, Damiano N, Cusano P, Di Vito MA, de Vita S, Del Pezzo E (2012) Subsurface structure of the Solfatara volcano (Campi Flegrei caldera, Italy) as deduced from joint seismic-noise array, volcanological and morphostructural analysis. Geochem Geophys Geosys 13(7):1-25. doi:10.1029/2011GC004030

Richards K, Revil A, Jardani A, Henderson F, Batzle M, Haas A (2010) Pattern of shallow ground water flow at Mount Princeton Hot Springs, Colorado, using geoelectrical methods. J Volzanol Geoth Res 198:217-232. doi:10.1016/j.jvolgeores.2010.09.001

Rosi M, Sbrana A (1987) Introduction, geological setting of the area, stratigraphy, description of mapped products, petrography, tectonics In: Rosi M, Sbrana A (eds) Phlegrean Fields. QRS 114(9) CNR, Rome, pp 9-93. ISBN:451

Sasaki Y (1994) 3D resistivity inversion using the finite-element method. Geophysics 59:1839-1848. doi:10.1190/1.1443571

Shima H (1990) Two-dimensional automatic resistivity inversion technique using alpha centers, Geophysics 55:682-694. doi:10.1190/1.1442880

Skeels DC (1963) An approximate solution of the problem of maximum depth in gravity interpretation. Geophysics 28:724-735. doi:10.1190/1.1439262

Soupios PM, Vallianatos F, Papadopoulos I, Makris JP, Marinakis M (2005) Surface-geophysical investigation of a landfill in Hania, Crete. In: Agiountantis Z, Komnitsas K (eds) International Workshop Geoenv 2005. Heliotopos Conferences, Athens, pp 149-156. ISBN:960-881-53-7-1

Soupios PM, Papadopoulos I, Kouli M, Georgaki I, Vallianatos F, Kokkinou E (2007) Investigation of waste disposal areas using electrical methods: a case study from Chania, Crete, Greece. Environ Geol 51:1249-1261. doi:0.1007/s00254-006-0418-7

Todesco M, Chiodini G, Macedonio G (2003) Monitoring and modelling hydrothermal fluid emission at La Solfatara (Phlegraean Fields, Italy). An interdisciplinary approach to the study of diffuse degassing. J Volcanol Geoth Res 125:57-79. doi:10.1016/S0377-0273(03)00089-1

Todesco M, Berrino G (2005) Modelling hydrothermal fluid circulation and gravity signals at the Phlegrean Fields caldera. Earth Planet Sci Lett 240:328–338. doi:10.1016/j.epsl.2005.09.016

Tripp AC, Hohmann GW, Swift CM (1984) Two-dimensional resistivity inversion. Geophysics 49:1708-1717. doi:10.1190/1.1441578

Troiano A, Petrillo Z, Di Giuseppe MG, Balasco M, Diaferia I, Di Fiore B, Siniscalchi A, Patella D (2008) About the shallow resistivity structure of Vesuvius volcano. Ann Geophys 51:181-189. doi:10.4401/ag-3043

Troiano A, Di Giuseppe MG, Petrillo Z, Troise C, De Natale G (2011) Ground deformation at calderas driven by fluid injection: modelling unrest episodes at Campi Flegrei (Italy). Geophys J Int 187:833-847. doi:10.1111/j.1365-246X.2011.05149.x

Troiano A, Di Giuseppe MG, Patella D, Troise C, De Natale G (2014) Electromagnetic outline of the Solfatara-Pisciarelli hydrothermal system, Campi Flegrei (Southern Italy). J Volcanol Geoth Res 277:9-21. doi:10.1016/j.jvolgeores.2014.03.005

Van Zijl JSV (1985) A practical manual on the resistivity method. Geophysics Division Nat. Phys. Res. Lab., Counc. Sci. Ind. Res., South Africa

Vargemezis G (2014) 3D geoelectrical model of geothermal spring mechanism derived from VLF measurements: A case study from Aggistro (Northern Greece). Geothermics 51:1-8. doi:10.1016/j.geothermics.2013.09.001

Ward SH (1990) Resistivity and induced polarization methods. In: Ward SH (ed) Geotechnical and Environmental Geophysics, Vol.I: Review and Tutorials. Investigations in Geophysics 5 SEG, Tulsa, pp 147-189. ISBN:978-0-931830-99-0

Wardman JB, Wilson TM, Bodger PS, Cole JW, Johnston DM (2012) Investigating the electrical conductivity of volcanic ash and its effect on HV power systems. Phys Chem Earth A 45-46: 128-145. doi:10.1016/j.pce.2011.09.003

Xia J, Ludvigson G, Miller RD, Mayer L, Haj A (2010) Delineation of a volcanic ash body using electrical resistivity profiling. J Geophys Eng 7:267–276. doi:10.1088/1742-2132/7/3/005

Zeyen H, Pessel M, Ledésert B, Hébert R, Bartier D, Sabin M, Lallemant S (2011) 3D electrical resistivity imaging of the near-surface structure of mud-volcano vents. Tectonophysics 509:181-190. doi:10.1016/j.tecto.2011.05.007

FIGURE CAPTIONS

Fig. 1 Digital elevation map of the Campi Flegrei composite caldera (Southern Italy). The red box includes the Solfatara crater, where the ERT survey was carried out.

Fig. 2 Aerial photo of the Solfatara crater. The white area is the vegetation-free degassing area. The black diamonds labelled BG, BN, LS and LF indicate the *Bocca Grande* (Big vent), *Bocca Nuov*a (New vent), *Le Stufe* (Stoves) and *La Fangaia* (Mud pool) main fumarole fields, respectively, in the crater. The yellow lines numbered from 1 to 8 indicate the new ERT profiles. The cyan dashed line indicates the western half of the CSAMT-MT profile discussed in Troiano et al. (2014).

Fig. 3a Apparent resistivity pseudosections across the profiles ERT1, ERT2, ERT4, ERT5, ERT6 and ERT7 reported in Fig.2.

Fig. 3b Apparent resistivity pseudosections across the profile ERT3 and ERT8 reported in Fig.2.

Fig. 4 Horizontal slices of the near-surface resistivity pattern beneath the Solfatara crater at six different depths, constructing using the 3D PERTI algorithm. The vertical level of the slices is given as depth below ground level, taking an x,y reference plane coincident with the flat central area of the crater, placed at 93 m asl, and (in parentheses) directly as height above sea level. For clarity, the ERT profiles in fig.2 are drawn with dashed lines in the top slice. Along the colour scale the subdivision in low, intermediate and high resistivity classes, LR, IR and HR, respectively, is reported.

Fig. 5 Horizontal slices of the near-surface resistivity pattern beneath the Solfatara crater at six different depths, deduced by interpolating the model data obtained along each individual profile by applying the RES2DINV algorithm. The style used to represent the maps is the same as in Fig.5.

Fig. 6 Horizontal slices at increasing pseudodepth, showing the pattern of the modulus of the discrepancy index, calculated as the difference between the field and simulated apparent resistivity values, divided by the simulated apparent resistivity. In the slices, z stands for pseudodepth, unlike in maps of Fig.4 and Fig.5, where it is depth. The field apparent resistivity dataset includes the measured apparent resistivity values and those extrapolated from them in all of the points not sensed by the ERT array, down to the maximum pseudodepth of 80 m. The simulated apparent resistivity dataset has been derived from the PERTI model depicted in Fig.4.

Fig. 7 3D perspective, viewed vertically upward, of the link between the CSAMT-MT depth section obtained by Troiano et al. (2014) with 80 mbgl slice extracted from the the 3D ERT model slice for 80 mbgl (Fig. 5f) presented in this paper. The line of intersection of the two cross sections corresponds with the trace of the CSAMT-MT profile, drawn with a cyan dashed line in Fig.2.

Fig. 8 CO_2 flux, soil temperature and Bouguer anomaly contour lines superimposed onto a synthetic 3D version of the PERTI model. The bluish and reddish volumes represent the LR ($\rho \le 4$ Ωm) and HR ($\rho \ge 60$ Ωm) resistivity classes, respectively. The white area includes the whole IR class (5 Ωm $\le \rho \le$ 50 Ωm).

Comment [A9]: This is confusing – the "3D ERT" model is shown as a single (2D) plane; whic plane? Is it the sum of all planes?

Fig. 9 Estimation of the depth to the centres of the sources of the two gravity lows appearing in the Bouguer map within the Solfatara crater, under the simplifying assumption that the causative bodies have spherical symmetry. The two radial lines A-A' and B-B' have been selected through the centres of the minima, nearly along the trend direction of the field (regional gravity). Nettleton's approximate approach (Nettleton 1971) has been used, consisting of: (1) tracing the estimated trend profile, which has been assumed to be linear (red straight-line in both the bottom diagrams); (2) plotting the gravity anomaly values (green full circlets) extracted from the Bouguer contour drawing (top map); (3) plotting the residual gravity anomaly values (blue full circlets) using the trend line as zero level; (4) computing and drawing, by trial-and-error, the synthetic sphere effect curve (red full ellipses) matching the gravity residual plots; (5) finding the horizontal distance $2x_{1/2}$ between the symmetrical points where the residual anomaly is half the value at its centre.

Electrical resistivity tomography imaging of the near-surface structure of the Solfatara crater, Campi Flegrei (Naples, Italy)

M.G. Di Giuseppe[1*], A. Troiano[1], A. Fedele[1], T. Caputo[1], D. Patella[2], C. Troise[1], G. De Natale[1]

[1] Istituto Nazionale di Geofisica e Vulcanologia (INGV), Osservatorio Vesuviano, Naples, Italy.

[2] Department of Physics, University Federico II, Naples, Italy.

[*] Corresponding author e-mail: mariagiulia.digiuseppe@ov.ingv.it

Abstract

We describe the results from an electrical resistivity tomography (ERT) survey performed inside the Solfatara crater, located in the central part of the Campi Flegrei (CF) composite caldera. The Solfatara volcano represents the most active zone within the CF area, in terms of hydrothermal manifestations and local seismicity. Eight dipole-dipole ERT lines have been measured with the aim of deducing a 3D resistivity model for the upper 80 m beneath the Solfatara. The results have allowed classification of the shallow structure below the crater into a low-resistivity (LR) class, up to about 4 Ωm, an intermediate resistivity (IR) class, from 5 Ωm up to 50 Ωm, and a high-resistivity (HR) class, from 60 Ωm onward. In order to solve the ambiguities arising in the interpretation of the nature of these bodies, a comparison has been done between the 3D ERT model and the CO_2 flux, soil temperature and gravity maps over the same area. By combining all of these parameters, the whole LR body has been ascribed to a water-dominated geothermal basin and the HR body to a steam/gas-dominated reservoir. Finally, the IR class has been interpreted as a widespread background situation with intermediate character, where volatiles and condensates can coexist in the same volumes at variable percentages, coherently with the resistivity variation within this class. Since fluid dynamics in the Solfatara crater change rapidly, ERT surveys repeated in the future are expected to be of great help in monitoring possible pre-eruptive changes, as well as in better following evolution of the local geothermal system.

Keywords: Campi Flegrei, Solfatara crater, near-surface structure, 3D resistivity tomography

Introduction

The Campi Flegrei (CF) caldera (Fig.1) was formed by huge eruptions 39000 and 15000 years ago (Rosi and Sbrana 1987). Vertical ground movements with rates from centimeters to meters per year characterize the dynamics of this area even during quiescent periods (Dvorak and Mastrolorenzo 1991). Since 1969, the area has been in a new phase of uplift after several centuries of subsidence dating back to 1538, when the last eruption occurred in the area (Di Vito et al. 1987). The most recent episodes of

1 intense ground deformation are the two unrests of 1970-72 and 1982-84, causing a

2 cumulative maximum uplift of over 3.5 m, accompanied by intense seismicity. All of

3 the recent literature on the interpretation of such uplift episodes points out the driving

4 role that fluid dynamics and related phase transformation processes have in the area,

5 especially where hydrothermal manifestations are most evident (e.g. De Natale et al.

6 1991; Chiodini et al. 2003; De Natale et al. 2006; Troiano et al. 2011).

7 The Solfatara crater (fig.1) represents the most active zone within the CF

8 caldera. Its activity has long been considered a direct indicator of the volcanic

9 dynamics taking place in the whole caldera. The crater has in fact been the site of

10 intense hydrothermal activity since Greek times, and currently exhibits impressive

11 degassing manifestations. A direct relationship has always been observed between

12 increases in hydrothermal activity in the Solfatara area and ground uplift in the CF

13 caldera.

14 As is well known, geophysics has a prominent role in volcanology. The

15 geophysical mapping of the Solfatara structure is a crucial step for improving our

16 ability to forecast pre-eruptive scenarios, as well as for estimating its geothermal

17 potential. Electrical and electromagnetic (EM) methods are among the most suitable

18 tools, thanks to the large variability and great diagnostic power of the resistivity

19 parameter in volcano-geothermal areas.

20 Only recently, the Solfatara volcano has begun to be surveyed by geoelectrics

21 (Bruno et al. 2007), controlled source audiomagnetotellurics (CSAMT) and natural

22 source magnetotellurics (MT) (Bruno et al. 2007; Troiano et al. 2014). A summary of

23 these results combined with those from gravity and seismic surveys will be given in

24 the next section. What is essential to stress now is that, while the large-scale structure

25 of the volcano, down to a few kilometers depth, has been fairly well imaged across

26 two CSAMT-MT orthogonal profiles, the shallow subsurface of the crater, down to 60

27 m depth, has been only approximately outlined by a 2D inversion of four electrical

28 resistivity tomography (ERT) lines (Bruno et al. 2007). Thus, in order to construct a

29 3D resistivity model of the Solfatara near-surface hydrothermal system, eight new

30 ERT lines were measured in 2013, distributed over the accessible area of the crater

31 (Fig. 2).

1   In the following sections, after providing a geophysical outline of the Solfatara

2   volcano based on previous investigations, results from the new ERT survey will be

3   presented and discussed.

4   **Geophysical outline of Solfatara**

5   The Solfatara volcano (Fig.1) is located inside the CF caldera, about 2 km ENE of the

6   town of Pozzuoli. It is a tuff cone formed 3700-3900 years ago, which in 1198 AD

7   generated a low-magnitude explosive eruption that ejected tephra over a small area (<1

8   km^2) (Di Vito et al. 1999). The crater is made up of a phreatic-magmatic breccia

9   overlain by a sequence of pyroclastic flow deposits, mostly altered by fumarolic

10   activity. It has a nearly elliptical shape with diameters of 580 m and 770 m, and the

11   highest relief along its rim reaches 199 m asl.

12   The Solfatara crater is located very close to the area of maximum ground uplift

13   and is the most active seismic area. It hosts large and spectacular fumarole vents

14   (Fig.2), with maximum flow temperatures in the range 150-160°C at the *Bocca*

15   *Grande* (BG) and *Bocca Nuova* (BN) fumaroles and about 100°C at *Le Stufe* (LS) and

16   *La Fangaia* (LF) ones (Chiodini et al. 2001). Systematic measurements of the gas

17   fluxes from the soil indicate up to 1500 tons/day of CO_2 emission through the main

18   fault system and temperature up to 95°C far from the fumaroles (Granieri et al. 2010).

19   At the LF area, in the west, and the BN and BG areas in the east (Fig.2), anomalously

20   high CO_2 discharge and high seismic noise have been monitored from 2000 to date.

21   Except for the pioneering gravity survey by Oliveri del Castillo et al (1968), the

22   crater has only recently become the site of detailed geophysical prospecting

23   campaigns. Petrosino et al. (2012) obtained an image of the shallow crustal structure

24   of Solfatara by correlating the local seismic noise with the results of a volcanological

25   and morphostructural survey. They observed a coherent, high degree of heterogeneity

26   in shear wave velocity, reflecting lithological contrasts and the structural setting. Their

27   conclusion was that the volcanic edifice was generated by a complex alternation of

28   constructive and destructive phases from an eruptive vent migrating eastwards,

29   subsequently affected by rainfall and altered by hydrothermal activity. Letort et al.

30   (2012) inferred the main subsurface features of the Solfatara crater by correlating

31   active and passive seismic data with CO_2 flux and soil temperature maps. In particular,

1 they were able to define the properties of a near-surface body, localized near the mud

2 pool area (LF area in Fig.2), associated with the top part of a hydrothermal system

3 plume.

4   Bruno et al. (2007), integrating near-surface TDEM, ERT and seismic profiles

5 with hydrogeological investigations, approximated the subsoil beneath the crater,

6 down to about 60 m depth bgl, as a two-layer sequence. The top layer with average

7 thickness around 20 m was associated with a dry argillitic alteration zone affected by

8 CO_2 degassing. The underlying zone was inferred to be associated with a

9 hydrothermal aquifer recharged by natural condensates through faulted and/or

10 fractured blocks affected by the expulsion of gas-rich hydrothermal fluid.

11   The deeper structure below the Solfatara crater has also been investigated by

12 CSAMT and MT data. Bruno et al. (2007) analyzed a set of 6 CSAMT-MT soundings,

13 along a N-S-profile on the western side of the crater, deducing that west of the LF area

14 the hydrothermal aquifer extends down to 300-400 m at least, below the ground

15 surface. Most recently, Troiano et al. (2014) have shown the results from a 3D

16 inversion of a combined CSAMT-MT nearly E-W, 1.2 km long profile in the Solfatara

17 crater and adjacent Pisciarelli area (Fig.1), crossing the CSAMT-MT line by Bruno et

18 al. (2007) west of the LF area (Fig.2). Below the Solfatara crater, Troiano et al. (2014)

19 found a 1-10 Ωm conductive body localized west of the LF area and extending from

20 ground surface down to 300-400 m, which was ascribed to a water-saturated, high-

21 pressure geothermal reservoir, in agreement with the finding by Bruno et al. (2007) for

22 the same area. Troiano et al. (2014) highlighted, near Solfatara's eastern rims, a nearly

23 vertical, 50-90 Ωm resistive plumelike structure escaping at about 2 km depth from the

24 top edge of a presumably horizontal, slightly more resistive platelike body. The

25 plumelike structure reaches the free surface where the BN and BG fumarole fields are

26 active (Fig.2), whereas the platelike structure extends at least down to the 3 km

27 maximum depth of EM exploration. Based on *P*-to-*S* wave velocity ratios, gravity and

28 geochemical data, the plumelike portion has been interpreted as a steam/gas-saturated

29 column and the platelike portion to a high temperature (>300°C), over-pressured, gas-

30 saturated reservoir.

31 **The ERT survey in the Solfatara crater**

1   As previously said, the resistivity parameter varies strongly, allowing the great

2   majority of buried structures of volcanological and geothermal interest to be

3   distinguished. The ERT approach can greatly enhance the resolution. It involves

4   acquisition of large datasets, which can now be quickly collected using computer-

5   assisted, multichannel resistivity meters. Refined 2D and 3D inversion codes (e.g.

6   Tripp et al. 1984; Shima 1990; Park and Van 1991; Li and Oldenburg 1992; Sasaki

7   1994; Loke and Barker 1995; Dahlin and Zhou 2004; Mauriello and Patella 2009)

8   further strengthen ERT, making it very effective for imaging volcanic structures down

9   to a few hundred meters depth (e.g. Di Maio et al. 1997; 1998a; Bruno et al. 2007;

10 Legaz et al. 2009; Zeyen et al. 2011; Fikos et al. 2012).

11   Eight ERT profiles have been acquired in the Solfatara crater (Fig.2) using a

12 Dipole-Dipole (DD) electrode configuration with a full array of maximum 72

13 electrodes. In confined areas where it was difficult to manage cable layouts, as in the

14 Solfatara crater, we found it effective to use the DD source-receiver coupling, because

15 it is more compact and is both sensitive to lateral location and facilitates depth

16 evaluation of anomaly source bodies (Ward 1990). For the source we used the IRIS

17 Syscal Pro system with maximum output voltage and current of 800 V and 2 A,

18 respectively. Six 230 m long profiles (ERT1, ERT2, ERT4, ERT5, ERT6 and ERT7)

19 were characterized by a minimum electrode spacing of 5 m and maximum depth of

20 penetration of about 40 m. Two 550 m long profiles (ERT3 and ERT8), each

21 composed of two overlapping segments, were also realized, characterized, instead, by

22 a 10 m minimum electrode spacing and maximum depth of penetration of about 80 m.

23   The apparent resistivity pseudosections across the ERT1, ERT2, ERT4, ERT5,

24 ERT6 and ERT7 profiles are drawn in Fig.3a, those across the ERT3 and ERT8

25 profiles in Fig.3b. Pseudosection plots are obtained by contouring the apparent

26 resistivity values and are a convenient means to display the data, but have only a rough

27 relationship with the real resistivity pattern. Shape and amplitude of the anomalies,

28 which strictly represent shifts among different apparent resistivity values, depend on

29 the unknown true resistivity pattern and data density, and also on contamination due to

30 even small inhomogeneities close to electrodes. We have used the criterion of placing

31 the vertical position of the plotting point at the median depth of investigation, or

32 pseudodepth, of the DD array (Edwards 1977).

1 An inspection of the eight pseudosections reveals, along all of the profile

2 directions, diffuse lateral and vertical heterogeneities within an apparent resistivity

3 range of about 2.5 orders of magnitude. Sometimes, sharply different results are

4 obtained in the same pseudodepth range between nearby profiles. The most striking of

5 such effects is the red spot with apparent resistivity values ranging between 20 Ωm

6 and 100 Ωm, appearing in the distance range 120-160 m and pseudodepth range 20-40

7 m along the ERT5 profile. Nothing similar is evident along the nearby ERT7 profile,

8 where, instead, apparent resistivity values are around 8 Ωm in almost the same

9 inspected volume. Effects like this are not surprising when using the DD electrode

10 array, because this array is very sensitive to electrode effects and invariably produces

11 ERT graphs with a large scatter in the measured points (Van Zijl 1985; Ward 1990).

12 In conclusion, we infer strong 3D inhomogenities in the near-surface structure of

13 the crater. It was thus felt necessary to proceed with a full 3D inversion of all of the

14 ERT profiles. To accomplish this aim, we use the PERTI method (Mauriello and

15 Patella 2009), which is a very fast, user-friendly inversion tool, quite appropriate for

16 dealing with a great multiplicity of data sets collected along even randomly oriented

17 profiles. For the interested reader, an outline of the PERTI theory is given in the

18 appendix.

19 **The 3D resistivity model of the Solfatara crater**

20 We show now the results obtained from the application of the PERTI algorithm to the

21 whole ERT data set, collected along the lines drawn in Fig.2. Six resistivity maps at

22 different depths have been plotted (Fig.4). In all of the maps, the depth is referred to

23 the zero level taken in correspondence with the flat ground surface in the large central

24 area of the crater, at 93 m mean altitude above sea level. We stress that the shallower

25 maps are much better resolved than the deeper ones, thanks to the much greater

26 number of datum points available within the pseudodepth range from ground surface

27 down to 40 m. The deeper maps, in fact, are constrained by a number of datum points

28 that rapidly decreases from 40 m down to 80 m, since this pseudodepth range has been

29 reached only by the two nearly orthogonal profiles ERT3 and ERT8 on gradually

30 shorter segments. A consequence of this is that in all of the points of the two deeper

1 maps at 60 m and 80 m bgl in Fig.4, lacking any measured apparent resistivity values,

2 the PERTI tool has just linearly predicted resistivity.

3 Since this is the first application of the PERTI tool to volcanology, the ideal

4 approach for assessing the confidence level of its results is to compare them with those

5 derived from a standardised program, like the renowned RES3DINV and ERTlab 3D

6 commercial softwares, as was done in some recent applications to archaeology

7 (Cozzolino et al. 2012; 2014). The difficulty, however, is that we could not directly

8 apply any of those programs to the present case, because of the random directions of

9 the profiles. Therefore, we decided to use for comparison the approximate model

10 resulting from the 3D interpolation of the single 2D inversions of the ERT profiles

11 obtained using the RES2DINV program.

12 Fig.5 shows the approximate model thus derived, using the same sequence of

13 maps as for the PERTI model in Fig.4. The comparison between the two models

14 shows an overall structural similarity in terms of the gross geometrical features, as

15 well as the resistivity range that characterizes the whole surveyed area. The main

16 difference is in the shapes of the boundaries of the bodies, which in Fig.5 are

17 considerably affected by spurious dragging effects due to the interpolation process,

18 which creates adjacent bodies with improbably strongly contrasting resistivity. We

19 consider the risk of generating artefacts is higher when using a 3D reconstruction from

20 2D inversions, because interpolation based on 2D inversion models necessarily rubs

21 out details between profiles. We are confident that the PERTI model in Fig.4 provides

22 a reasonable solution to the 3D inversion problem of the Solfatara database.

23 To support this conclusion we illustrate the results from the analysis of the

24 degree of similitude between the field apparent resistivity dataset and the simulated

25 apparent resistivity dataset derived from the PERTI model of Fig.4, using a subroutine

26 of the RES3DINV software apt to solve the direct problem. The degree of similitude

27 has been quantified using the dimensionless discrepancy index, $d(\mathrm{P}_i)$, given as

28 $$d(\mathrm{P}_i) = \frac{\rho_{a,f}(\mathrm{P}_i) - \rho_{a,s}(\mathrm{P}_i)}{\rho_{a,s}(\mathrm{P}_i)}, \quad i = 1, 2, ..., N, \tag{1}$$

29 where $\rho_{a,f}(\mathrm{P}_i)$ and $\rho_{a,s}(\mathrm{P}_i)$ are the field apparent resistivity and the simulated apparent

30 resistivity, respectively, both assigned at the same i-th attribution point P_i, and N is the

31 total number of attribution points. It is easy to verify that $d(\mathrm{P}_i) \in \,]-1, +\infty[$. Fig.6 shows a

1 sequence of maps at increasing pseudodepths, where the modulus of the discrepancy

2 index is contoured. Apart from a negligible number of points (reddish points in Fig.6),

3 where $|d(P_i)|$ is exceedingly high, from 1 up to 1.5, and a few small areas (yellowish

4 areas), where $|d(P_i)|$ varies around 0.6, in all of the slices $|d(P_i)|$ appears clustered in

5 two subsets. In the first subset, which includes all of the greenish areas, $|d(P_i)|$ varies

6 around 0.3, while in the second subset, which includes all of the bluish areas, $|d(P_i)|$

7 ranges between 0 and 0.15.

8 The $d(P_i)$ dataset can be used to estimate the RMS error, defined as (e.g. Feng et

9 al. 2014; Loke 2014)

10 $$\text{RMS} = \sqrt{\frac{\Delta r^T \Delta r}{N}}, \qquad (2)$$

11 where Δr is the data residual vector, namely, the difference of the *N*-dimensional

12 vector with components $\log[\rho_{a,f}(P_i)]$ and the *N*-dimensional vector with components

13 $\log[\rho_{a,s}(P_i)]$, with the superscript *T* denoting transposition. Using the definition in eq.1,

14 after a few simple mathematical steps, one obtains

15 $$\text{RMS} = \sqrt{\frac{\sum_{i=1}^{N}\{log[1+d(P_i)]\}^2}{N}}. \qquad (3)$$

16 By inserting in eq.3 the $d(P_i)$ dataset, whose modulus is plotted in Fig.6, we obtained a

17 percent RMS error of 13.26%. This is a fairly satisfactory result from the very fast

18 one-step PERTI algorithm, if one considers the great logistical difficulties and the

19 highly heterogeneous resistivity distribution within the crater. It must also be stressed

20 that RMS errors of this order of magnitude, and even much greater, are quite often

21 found in 3D resistivity environments, in different research fields, even when using

22 sophisticated, iterative inversions (e.g. Lapenna et al. 2003; Soupios et al. 2005; 2007;

23 Athanasiou et al. 2007; Giocoli et al. 2008; Aizebeokhai et al. 2010; Ortega et al.

24 2010; Richards et al. 2010; Loke 2014; Vargemezis 2014).

25 Turning back to the maps in Fig.4, their overall coherence was considered

26 sufficient to attempt a 3D zoning in terms of resistivity classes. We started with a

27 visual inspection of the maps, taking into account the conceptual model of the area

28 based on volcanological data. Key aspects of this conception are the widespread

1 pyroclastic nature of the surface layer, the diffuse degassing throughout the area, and

2 the presence of a large mud pool, on one side, and vigorous fumarole vents on the

3 other side. These features are all developed in an environment of continual changes

4 caused by the uprising of aggressive hydrothermal fluids of deep origin, self-sealing

5 processes and opening of cracks and fractures. In the maps we note a general low-to-

6 medium resistivity context: resistivity reaches values as low as 1 Ωm, on one side, and

7 does not exceed 200 Ωm, on the other side. The larger detected high resistivity body

8 appears, in fact, to effectively coincide with the BN and BG fumarole vents, while the

9 low resistivity volumes appear to surround the LF area.

10 We also rely on previously published results, though only a few are available

11 (e.g. Byrdina et al. 2014; Di Maio et al. 1998b; Bruno et al. 2007; Troiano et al. 2008;

12 Legaz et al. 2009; Xia et al. 2010; Zeyen et al. 2011; Fikos et al. 2012; Wardman et al.

13 2012). The ways used to classify the resistivity ranges are quite similar. In this regard,

14 we note that volcanic environments in different places, even if phenomenologically

15 comparable, would not have had identical evolution and physicochemical

16 development.

17 Based on these facts, the following three different classes have been identified.

18 The first class, referred to as a low resistivity (LR) class, includes bodies with

19 resistivity ≤4 Ωm, corresponding in Fig.4 with the contoured patches from light blue

20 to violet. In the deeper maps, the LR class occupies a large portion of the SW

21 quadrant. Looking at the shallower maps, the LR class includes a fragmented, arcuate

22 sequence of spots around a wide central part of the crater, which corresponds with the

23 mud pool area (LF area in Fig.2). Of this sequence, the segments in the west and north

24 appear of much larger extent, especially at 30 m depth bgl, while the southern branch

25 is made of smaller, separated spots, which clearly appear only in the map at 40 m bgl.

26 The second class, which we call the high resistivity (HR) class, includes all

27 bodies that have resistivity values ≥60 Ωm, corresponding in Fig.4 with the contoured

28 patches from dark orange to deep red. In the three deeper maps we observe that the

29 HR class includes a rather uniform body situated in the southeast quadrant. Proceeding

30 upwards, this body vanishes, but a small HR channel seems to emerge out of it, rising

31 up to near surface, as documented by the red spot appearing at the eastern margin of

32 the SE quadrant of the three shallower maps. It is also interesting that there is a HR

1 volume along the northern margin of the area, clearly visible from 30 m bgl upwards.

2 Finally, we note the presence of a cluster of small red spots only in the maps at z=20 m

3 and z=30 m bgl, located in correspondence with the southern border of the mud pool,

4 with resistivity around the lower limit of the HR-class.

5   The third class, which we call the intermediate resistivity (IR) class, includes all

6 bodies that have resistivity values between 5 Ωm and 50 Ωm, corresponding in Fig.4

7 with the contoured areas from deep green to brownish yellow.

8 **Discussion**

9 We now proceed to interpretation of the model depicted in Fig.4. First we show (Fig.

10 7) a 3D perspective view of the link between the CSAMT-MT section inferred by

11 Troiano et al. (2014) along with the PERTI section slice at z=80 m bgl, viewed from

12 the bottom,from the 3D ERT model presented in this paper. The line of intersection of

13 the two cross sections corresponds with the trace of the CSAMT-MT profile, drawn

14 with a cyan dashed line in Fig.2. With respect to the general resistivity pattern, the

15 correspondence along the junction line appears, at a large scale, quite good. Since the

16 average distance between any two contiguous CSAMT station sites along the profile

17 was about 100 m, the uppermost portion of the CSAMT-MT depth section may be

18 looked at as a smoothed version of the ERT resistivity distribution along the junction

19 line. We recall now that the electrically conductive body localised west of the LF area

20 by the CSAMT-MT survey was ascribed by Troiano et al. (2014) to a water-saturated,

21 high-pressure geothermal reservoir. The resistive zone localised below the BG and BN

22 area was, in contrast, associated with a steam/gas-saturated column. Such

23 correspondences can be used as basic guidelines for the interpretation of the PERTI

24 model. Thus, referring to the LR ERT class, the large volume situated in the western

25 sector, and the smaller bodies all around at variable depth (Fig.4), can be ascribed to

26 porous, permeable rocks saturated with highly ionized condensates. For the HR ERT

27 class, the large volume situated in the eastern sector and all of the smaller bodies all

28 around, can instead be ascribed to fractured rocks saturated with volatiles.

29   As with the interpretation of the CSAMT-MT data by Troiano et al. (2014),

30 which they did by combining geochemical data, body wave velocity ratio and density

1 contrast, a similar approach can now be used to support the above preliminary PERTI

2 model interpretation. Here we consider the CO_2 flux and soil temperature maps

3 presented in Bruno et al. (2007) and the Bouguer anomaly map of Oliveri del Castillo

4 et al (1968).

5 Fig.8 shows the map of CO_2 flux superimposed on a top view of the resistivity

6 isosurfaces of the PERTI model. We observe in the central crater area a cluster of

7 closely spaced highs in CO_2 flux. What seems noteworthy is that the higher CO_2 peaks

8 occur within and west of the BN-BG area. In particular, the highest CO_2 peak appears

9 exactly in correspondence with the tube-like HR body arising from the deeper large

10 HR structure in the SE quadrant of the area. In contrast, the less intense CO_2 peaks

11 appear to correspond to those portions of the IR class where, at various depth levels,

12 the resistivity approaches the IR class top limit (see also Fig.4). Fig.8 shows also the

13 map of soil temperature superimposed on the PERTI model top view. Since this map

14 looks very similar to that of the CO_2 flux, the correspondence is the same as above.

15 This double comparison seems thus to confirm that within the HR resistivity class

16 there is a general predominance of high temperature volatiles. Condensate fluids

17 should, instead, dominate within the LR bodies, above which no CO_2 and temperature

18 peaks were detected. Lastly, the IR class may reasonably represent intermediate

19 geothermal situations, where both fluid phases coexist and the rock/fluid system

20 evolves to the LR class or the HR class, following the dynamics of the

21 temperature/pressure source field. In detail, predominance of condensates or volatiles

22 is likely to occur where resistivity approaches the bottom or top limit of the IR class,

23 respectively.

24 Finally, Fig.8 shows also the comparison of the Bouguer anomaly map with the

25 PERTI model. Despite the fact that the gravity survey was conducted more than 45

26 years ago, we feel it can give further useful information for the geothermal

27 interpretation of resistivity data.

28 The Bouguer anomaly map of the Solfatara crater is characterized by two gravity

29 lows located in the central area, aligned roughly W-E, each having broadly radial

30 symmetry. The less pronounced minimum to the west spatially correlates quite well

31 with the LR body under the mud pool and surrounding areas. On the other side, the

32 more pronounced minimum appears centered over a large portion of the IR

33 background, where the resistivity approaches the lower limit of the HR class (see

1   Fig.4). Only a portion of this gravity minimum correlates with the large volume of HR

2   class material to the east on the PERTI map. To quickly estimate the maximum-depth

3   sources (Bott and Smith 1958; Skeels 1963; Mauriello and Patella 2001) of these two

4   local gravity minima, we have applied Nettleton's formula for spherical bodies, viz.

5    $d=1.305x_{1/2}$ (Nettleton 1971; 1976). In this equation, d is the depth to the center of the

6   source body and $x_{1/2}$ is the half-amplitude width of the anomaly, *i.e.* the horizontal

7   distance from the center of the anomaly to the point where the anomaly is half the

8   value at its center. Referring to Fig.9, where all steps of the approximate interpretation

9   process are depicted, the maximum depths of about 100 m and 75 m bgl have been

10   estimated to be the centers of the west and east source bodies, respectively. Therefore,

11   we interpret the results of the gravity map assuming that its sources are located almost

12   at the same depth ranges as those of the LR body under the mud pool and surrounding

13   areas, on one side, and the large volume of the HR class, on the other side.

14   For the western, less-pronounced gravity low, qualitatively we can say that the

15   location of its source body appears to correspond with that of the LR volume under the

16   mud pool area. Given that a density decrease is consistent with the expected mass

17   reduction for a rock having an increased proportion of voids, filled with volatiles

18   and/or condensates, the combination of low resistivity and low density in the same

19   body does not contradict the previous conclusion that the LR volume may consist of a

20   hot, highly ionized water-dominated geothermal system.

21   The adjacent, stronger, gravity low is observed to be located at a depth where its

22   source body could be the HR volume under the BG and BN vigorous fumarole vents.

23   Furthermore, density is expected to be even lower for a steam/gas dominated system

24   than a water-dominated one (Todesco and Berrino 2005). Therefore, if it were not for

25   the horizontal shift eastwards of the bulk HR volume from this gravity low, one could

26   directly say that a lower density combined with a higher resistivity supports the

27   identification of the HR volume under the BG and BN vents as a hot steam/gas-

28   dominated system. To confirm this conclusion, we must admit that such a shift is the

29   result of a migration of the HR volume eastwards during the time between the gravity

30   survey and our survey. We infer that, over the course of the few past decades, some

31   amount of water might, for instance, have invaded spaces previously saturated with

32   steam/gas below the gravity minimum, at the same time as steam/gas fluxes were

1   invading voids opening to the east. It must be stressed in this regard that, east of the

2   crater, close to the outer slopes of the Solfatara volcano, about 600 m far from the BN

3   and BG fumarole vents, the Pisciarelli fumarole field has shown a notable increase of

4   activity since 2003 (Troiano et al. 2014).

5   The only gravity high appearing to north in the map, which to some extent

6   includes the roughly prismatic HR body located a few tens of meters depth below the

7   northern margin of the survey area, represents a concomitant increase in resistivity and

8   density. We ascribe this HR body to a fine-grained, more-compact block of the crater

9   basal breccia, based on the description of volcanic products mapped in the Solfatara

10   (Rosi and Sbrana 1987).

11   Before concluding, we briefly discuss the links between the previous

12   geoelectrical observations by Bruno et al. (2007) and our new ERT results. First, we

13   observe that there is general agreement about the resistivity range describing the near-

14   surface structure of the Solfatara crater, from a few Ωm up to some tens of Ωm.

15   Furthermore, the sequence of slices in Fig.4 shows that the electrical schematization of

16   the crater's subsoil in terms of two layers, hypothesized by Bruno et al. (2007), may be

17   justified from the point of view of the degree of inhomogeneity of the levels. In Fig.4,

18   in fact, the first 30 m of depth bgl appear laterally much more discontinuous than the

19   deeper horizons.

20   **Conclusion**

21   We have described results from an ERT survey performed inside the Solfatara crater,

22   located in the central part of the CF composite caldera, west of Naples, Italy. Eight DD

23   ERT profiles, irregularly aligned due to insurmountable obstacles inside the crater,

24   have been carried out with the aim of producing a 3D resistivity model of deposits in

25   the uppermost 80 m beneath the Solfatara. To this purpose, we have adopted the 3D

26   probability-based ERT inversion (PERTI) method, which has the great advantage of

27   being a very fast inversion tool, quite appropriate for dealing with a great multiplicity

28   of data sets, even when they are collected with randomly distributed profiles. The

29   application to the Solfatara crater has proved the PERTI approach can be used as a fast

30   deconvolution filter also in complex volcano-geothermal environments.

1   The results from the PERTI approach have highlighted a complex resistivity

2   pattern beneath the crater, which we have broken into three resistivity classes, namely

3   a low resistivity (LR) class ($\rho \leq 4$ Ωm), an intermediate resistivity (IR) class (5 Ωm $\leq$

4    $\rho \leq 50$ Ωm) and a high resistivity (HR) class ($\rho \geq 60$ Ωm). Comparison with previous

5   geophysical and geochemical maps of the crater area allows us to ascribe a low density

6   volume of the LR class, localized in the south-western sector of the crater where there

7   is a well-known mud pool (*La Fangaia*) area, to a highly ionized, water-dominated

8   geothermal reservoir. It has also allowed us to attribute a larger, lower density, volume

9   of the HR class, localized in the southeastern sector of the crater among the *Bocca*

10   *Grande* and *Bocca Nuova* main fumarole fields, to a steam/gas-dominated basin.

11   Finally, the IR class has been ascribed to a widespread background environment with

12   intermediate hydrothermal features, where volatiles and condensates can coexist in the

13   same volumes with variable percentages, consistent with the resistivity variations

14   within the class.

15   To conclude, it has been confirmed that resistivity is mostly conditioned by the

16   fluid phases in rocks, an resistivity analysis has the specific ability to distinguish

17   water-dominated from gas-dominated situations. Therefore, because fluid dynamics in

18   active volcano-geothermal areas change rapidly, we think repeated ERT surveys in the

19   Solfatara crater are important in monitoring possibly pre-eruptive resistivity changes,

20   and for better following evolution of the local geothermal system.

21   **Appendix**
22   **Outline of the PERTI method**

23   The 3D PERTI method was proposed by Mauriello and Patella (2009) in the framework of the
24   probability tomography theory, which is now briefly outlined in order to better introduce the
25   basic principle underlying the inversion algorithm.
26   Probability tomography was at first suggested for the self-potential method to identify
27   the places underground, where higher is the occurrence probability of the sources that cause
28   the anomalies detected on the ground (Patella 1997a; 1997b). In geoelectrics, a similar
29   approach was formulated to image the most probable location of the resistivity anomaly
30   source bodies, consisting in plotting the occurrence probability function $\eta(P_q)$, calculated at a
31   grid of points P_q (*q*=1,2,…,*Q*) below the ground surface by the formula (Mauriello and Patella
32   1999)

33   $\eta(P_q) = C_q \sum_{k=1}^{K} \sum_{j_k=1}^{J_k} [\rho_a(P_{j_k}) - \rho] \, \Psi(P_{j_k}, P_q).$

34   (A1)

35   In eq.A1, $\rho_a(P_{j_k})$ is the measured apparent resistivity at P_{j_k}, *i.e.* the j_k-th nodal datum point of
36   the *k*-th profile (j_k=1,2,…,J_k; *k*=1,2,…,*K*), ρ is the resistivity of a homogeneous, isotropic half-

1 space assumed as reference, or starting model, C_q is a positive-definite non null normalization
2 factor, given by

3 $$C_q = \left\{ \sum_{k=1}^{K} \sum_{j_k=1}^{J_k} \left[\rho_a(P_{j_k}) - \rho\right]^2 \cdot \sum_{k=1}^{K} \sum_{j_k=1}^{J_k} \Psi^2(P_{j_k}, P_q) \right\}^{-1/2}$$

4 (A2)

5 and $\Psi(P_{j_k}, P_q)$ is the j_k-th Frechet derivative referred to the reference model, also known as
6 the sensitivity function of the array. It physically describes the effect generated at P_{j_k} by a
7 small perturbation of the reference resistivity at P_q, under Born approximation (Loke and
8 Barker 1995; 1996; Mauriello and Patella 1999).

9 Including topography, the sensitivity function for the DD array is calculated as follows.
10 Taking a rectangular coordinate system with the *xy*-plane at mean sea level and the *z*-axis
11 upwards, and indicating with $\left(x_{j_k}^A, y_{j_k}^A, z_{j_k}^A\right)$, $\left(x_{j_k}^B, y_{j_k}^B, z_{j_k}^B\right)$ and $\left(x_{j_k}^M, y_{j_k}^M, z_{j_k}^M\right)$, $\left(x_{j_k}^N, y_{j_k}^N, z_{j_k}^N\right)$
12 the coordinates of the current electrodes A and B and potential electrodes M and N,
13 respectively, and with $\left(x_q^P, y_q^P, z_q^P\right)$ the coordinates of the model point P_q, $\Psi(P_{j_k}, P_q)$ is
14 explicated asFor (8), the authors may emphasize in the manuscript that the authors
15 interpret the results of gravitational survey assuming that the sources are located
16 almost at same locations although this assumption should be examined.

17 $$\Psi(P_{j_k}, P_q) = \frac{G_{j_k}}{4\pi^2} \cdot \left(L_{q,j_k}^{AM} - L_{q,j_k}^{AN} - L_{q,j_k}^{BM} + L_{q,j_k}^{BN}\right),$$ (A3)

18 where G_{j_k} is the geometrical factor of the DD array and

19 $$L_{q,j_k}^{AM} = \frac{\left(x_q^P - x_{j_k}^A\right)\left(x_q^P - x_{j_k}^M\right) + \left(y_q^P - y_{j_k}^A\right)\left(y_q^P - y_{j_k}^M\right) + \left(z_q^P - z_{j_k}^A\right)\left(z_q^P - z_{j_k}^M\right)}{\left[\left(x_q^P - x_{j_k}^A\right)^2 + \left(y_q^P - y_{j_k}^A\right)^2 + \left(z_q^P - z_{j_k}^A\right)^2\right]^{3/2} \left[\left(x_q^P - x_{j_k}^M\right)^2 + \left(y_q^P - y_{j_k}^M\right)^2 + \left(z_q^P - z_{j_k}^M\right)^2\right]^{3/2}}$$ (A4a)

20 $$L_{q,j_k}^{AN} = \frac{\left(x_q^P - x_{j_k}^A\right)\left(x_q^P - x_{j_k}^N\right) + \left(y_q^P - y_{j_k}^A\right)\left(y_q^P - y_{j_k}^N\right) + \left(z_q^P - z_{j_k}^A\right)\left(z_q^P - z_{j_k}^N\right)}{\left[\left(x_q^P - x_{j_k}^A\right)^2 + \left(y_q^P - y_{j_k}^A\right)^2 + \left(z_q^P - z_{j_k}^A\right)^2\right]^{3/2} \left[\left(x_q^P - x_{j_k}^N\right)^2 + \left(y_q^P - y_{j_k}^N\right)^2 + \left(z_q^P - z_{j_k}^N\right)^2\right]^{3/2}}$$ (A4b)

21 $$L_{q,j_k}^{BM} = \frac{\left(x_q^P - x_{j_k}^B\right)\left(x_q^P - x_{j_k}^M\right) + \left(y_q^P - y_{j_k}^B\right)\left(y_q^P - y_{j_k}^M\right) + \left(z_q^P - z_{j_k}^B\right)\left(z_q^P - z_{j_k}^M\right)}{\left[\left(x_q^P - x_{j_k}^B\right)^2 + \left(y_q^P - y_{j_k}^B\right)^2 + \left(z_q^P - z_{j_k}^B\right)^2\right]^{3/2} \left[\left(x_q^P - x_{j_k}^M\right)^2 + \left(y_q^P - y_{j_k}^M\right)^2 + \left(z_q^P - z_{j_k}^M\right)^2\right]^{3/2}}$$ (A4c)

22 $$L_{q,j_k}^{BN} = \frac{\left(x_q^P - x_{j_k}^B\right)\left(x_q^P - x_{j_k}^N\right) + \left(y_q^P - y_{j_k}^B\right)\left(y_q^P - y_{j_k}^N\right) + \left(z_q^P - z_{j_k}^B\right)\left(z_q^P - z_{j_k}^N\right)}{\left[\left(x_q^P - x_{j_k}^B\right)^2 + \left(y_q^P - y_{j_k}^B\right)^2 + \left(z_q^P - z_{j_k}^B\right)^2\right]^{3/2} \left[\left(x_q^P - x_{j_k}^N\right)^2 + \left(y_q^P - y_{j_k}^N\right)^2 + \left(z_q^P - z_{j_k}^N\right)^2\right]^{3/2}}$$ (A4d)

23 In practice, the average apparent resistivity is assumed as reference uniform resistivity
24 ρ. Hence, $\eta(P_q)$, which is a number between -1 and +1, is interpreted as an occurrence
25 probability measure of a resistivity deviation from ρ at P_q. Positive or negative values of
26 $\eta(P_q)$ give the occurrence probability of an increase or a decrease of resistivity, respectively.
27 Many field cases were dealt with using this approach, including the Italian volcanic
28 areas of Mt. Etna and Mt. Vesuvius (Mauriello et al. 2004; Mauriello and Patella 2008a;
29 2008b). In all cases, the mapping of $\eta(P_q)$ proved to be a reliable tool for outlining geometry
30 and location of the source bodies, compatibly with the available data set.
31 Using eq.A1, no information can, however, be deducted as to the real resistivity values
32 of the structures, geometrically defined by the analysis of the probability index $\eta(P_q)$. Just to
33 find a solution to this last problem that the PERTI method has been proposed. The basic
34 principle for the PERTI method is that the reference resistivity ρ must not be pre-assigned, but
35 assumed to be the unknown true resistivity value ρ_q at P_q. With such an assumption, $\eta(P_q)$
36 given in eq.A1 can be rewritten as

$$\eta\left(P_q\right) = C_q \sum_{k=1}^{K} \sum_{j_k=1}^{J_k} \left[\rho_a\left(P_{j_k}\right) - \rho_q\right] \Psi\left(P_{j_k}, P_q\right).$$

(A5)

The rationale for the PERTI approach is that if $\eta\left(P_q\right) = 0$ resulted at P_q, then the most probable resistivity would be there exactly ρ_q. Since it is always $C_q \neq 0$, the $\eta\left(P_q\right) = 0$ condition allows the following inversion formula to be derived (Mauriello and Patella 2009)

$$\rho_q = \frac{\sum_{k=1}^{K} \sum_{j_k=1}^{J_k} \rho_a\left(P_{j_k}\right) \Psi\left(P_{j_k}, P_q\right)}{\sum_{k=1}^{K} \sum_{j_k=1}^{J_k} \Psi\left(P_{j_k}, P_q\right)}.$$

(A6)

The most probable real resistivity ρ_q at P_q, compatibly with data accuracy and density and within the assumed first order Born approximation, is simply derived as the weighted average of the apparent resistivity values, using as weights the sensitivity function of the array. Thus, the PERTI formula of eq.A3 can easily be converted into a user-friendly algorithm, quite apt to combine a great multiplicity of large datasets.

The main features of the PERTI method, derived from many simulations and field tests (Mauriello and Patella 2009; Cozzolino et al. 2012; 2014), are: (i) independence from a priori information; (ii) absence of iterative processes; (iii) drastic reduction of computing time with respect to standard deterministic inversion tools, like RES3DINV and ERTlab, which may require extremely long time of several hours, compared with the few ten seconds of the PERTI software, to elaborate a set of several thousands data points on a conventional 1 GB RAM PC (Cozzolino et al. 2014); (iv) independence from data acquisition techniques and spatial regularity, unlike the above mentioned commercial softwares, which are designed to invert data collected with a rectangular grid of electrodes.

A direct consequence of not requiring a priori information and iterative processes is, for the PERTI method, the uselessness of the computation of the RMS error between measured and modelled apparent resistivity values. The RMS error, whatever is, cannot be lowered in any way within the PERTI theory. Nonetheless, the same tests have shown PERTI modelling results quite comparable with those from the mentioned commercial softwares (Mauriello and Patella 2009; Cozzolino et al. 2012; 2014).

Acknowledgements

References

Aizebeokhai AP, Olayinka AI, Singh VS (2010) Application of 2D and 3D geoelectrical resistivity imaging for engineering site investigation in a crystalline basement terrain, southwestern Nigeria. Environ Earth Sci 61:1481-1492. doi:10.1007/s12665-010-0464-z

Athanasiou EN, Tsourlos PI, Vargemezis GN, Papazachos CB, Tsokas GN (2007) Non-destructive DC resistivity surveying using flat-base electrodes. Near Surface Geophys 5:263-272. doi:10.3997/1873-0604.2007008

Bott MHP, Smith RA (1958) The estimation of the limiting depth of gravitating bodies. Geophys Prospect 6:1-10. doi:10.1111/j.1365-2478.1958.tb01639.x

Bruno PG, Ricciardi GP, Petrillo Z, Di Fiore V, Troiano A, Chiodini G (2007) Geophysical and hydrogeological experiments from a shallow hydrothermal system at Solfatara

Volcano, Campi Flegrei, Italy: Response to caldera unrest. J Geophys Res 112:B06201. doi:10.1029/2006JB004383

Byrdina S, Vandemeulebrouck J, Cardellini C, Legaz A, Camerlynck C, Chiodini G, Lebourg T, Letort J, Motos G, Carrier A, Bascou P (2014) Relations between electrical resistivity, carbon dioxide flux, and self-potential in the shallow hydrothermal system of Solfatara (Phlegrean Fields, Italy). Geophys Res Abs 16. EGU2014-5204.

Chiodini G, Frondini F, Cardellini C, Granieri D, Marini D, Ventura G (2001) CO_2 degassing and energy release at Solfatara volcano, Campi Flegrei, Italy. J Geophys Res 106(B8):16213-16221. doi:10.1029/2001JB000246

Chiodini G, Todesco M, Caliro S, Del Gaudio C, Macedonio G, Russo M (2003) Magma degassing as a trigger of bradyseismic events: The case of Phlegrean Fields (Italy). Geophys Res Lett 30:1434. doi:10.1029/2002GL016790

Chiodini G, Granieri D, Avino R, Caliro S, Costa A, Werner C (2005) Carbon dioxide diffuse degassing and estimation of heat release from volcanic and hydrothermal systems. J Geophys Res 110:B08204. doi:10.1029/2004JB003542

Cozzolino M, Di Giovanni E, Mauriello P, Vanni Desideri A, Patella D (2012) Resistivity tomography in the park of Pratolino at Vaglia (Florence, Italy). Archaeol Prospect 19:253-260. doi:10.1002/arp.1432

Cozzolino M, Mauriello P, Patella D (2014) Resistivity tomography imaging of the substratum of the Bedestan monumental complex at Nicosia, Cyprus. Archaeometry 56:331-350. doi:10.1111/arcm.12018

Dahlin T, Zhou B (2004) A numerical comparison of 2D resistivity imaging with 10 electrode arrays. Geophys Prospect 52:379-398. doi:10.1111/j.1365-2478.2004.00423.x

De Natale G, Pingue F, Allard P, Zollo A (1991) Geophysical and geochemical modeling of the Campi Flegrei caldera. J Volcanol Geoth Res 48:199-222. doi:10.1016/0377-0273(91)90043-Y

De Natale G, Troise C, Pingue F, Mastrolorenzo G, Pappalardo L, Battaglia M, Boschi E (2006) The Campi Flegrei caldera: unrest mechanisms and hazards. In: Troise C, De Natale G, Kilburn CRJ (eds) Mechanics of Activity and Unrest at Large Calderas. Geological Societyof London Special Publications 269, pp 25-45. doi:10.1144/GSL.SP.2006.269.01.03

Di Maio R, Mauriello P, Patella D, Petrillo Z, Piscitelli S, Siniscalchi A, Veneruso M (1997) Self-potential, geoelectric and magnetotelluric studies in Italian active volcanic areas. Ann Geophys 40:519-537. doi:10.4401/ag-3926

Di Maio R, Mauriello P, Patella D, Petrillo Z, Piscitelli S, Siniscalchi A (1998a) Electric and electromagnetic outline of the Mount Somma-Vesuvius structural setting. J Volcanol Geoth Res 82:219-238. doi:10.1016/S0377-0273(97)00066-8

Di Maio R, Gerundo M, Giammetti S, Patella D, Piscitelli S, Veneruso M (1998b) Vulcano: Self-potential mapping and dipolar geoelectric tomography. Acta Vulcanol 10:133-136. ISSN:1121-9114

Di Vito MA, Lirer L, Mastrolorenzo G, Rolandi G (1987) The 1538 Monte Nuovo eruption (Campi Flegrei, Italy). Bull Volcanol 49: 608-615. doi:10.1007/BF01079966

Di Vito MA, Isaia R, Orsi G, Southon J, D'Antonio M, De Vita S, Pappalardo L, Piochi M (1999) Volcanism and deformation since 12,000 years at the Campi Flegrei caldera (Italy). J Volcanol Geoth Res 91:221-246. doi:10.1016/S0377-0273(99)00037-2

Dvorak JJ, Mastrolorenzo G (1991) The mechanisms of recent vertical crustal movements in Campi Flegrei caldera, Southern Italy. GSA Special Papers 263, pp 1-47. doi:10.1130/SPE263-p1

Edwards LS (1977) A modified pseudosection for resistivity and induced-polarization. Geophysics 42:1020-1036. doi:10.1190/1.1440762

Feng D, Dai Q, Xiao B (2014) Contrast between 2D inversion and 3D inversion based on 2D high-density resistivity data. Trans Nonferrous Met Soc China 24:224-232. doi:10.1016/S1003-6326(14)63051-X

Fikos I, Vargemezis G, Zlotnicki J, Puertollano JR, Alanis PB, Pigtain RC, Villacorte EU, Maliport GA, Sasai Y (2012) Electrical resistivity tomography study of Taal volcano hydrothermal system, Philippines. Bull Volcanol 74:1821-1831. doi:10.1007/s00445-012-0638-5

Giocoli A, Magrì C, Vannoli P, Piscitelli S, Rizzo E, Siniscalchi A, Burrato P, Basso C, Di Nocera S (2008) Electrical Resistivity Tomography investigations in the Ufita Valley (Southern Italy). Ann Geophys 51:213-223. doi:10.4401/ag-4443

Granieri D, Avino R, Chiodini G (2010) Carbon dioxide diffuse emission from the soil: ten years of observations at Vesuvio and Campi Flegrei (Pozzuoli), and linkages with volcanic activity. Bull Volcanol 72:103–118. doi:10.1007/s00445-009-0304-8

Lapenna,V, Lorenzo P, Perrone A, Piscitelli S, Sdao F, Rizzo E (2003) High-resolution geoelectrical tomographies in the study of Giarrossa landslide (southern Italy). Bull Eng Geol Env 62:259–268. doi:10.1007/s10064-002-0184-z

Legaz AV, Vandemeulebrouck JR, Revil A, Kemna A, Hurst AW, Reeves R, Papasin R (2009) A case study of resistivity and self-potential signatures of hydrothermal instabilities, Inferno Crater Lake, Waimangu, New Zealand. Geophys Res Lett 36:L12306. doi:10.1029/2009GL037573

Letort J, Roux P, Vandemeulebrouck J, Coutant O, Cros E, Wathelet M, Cardellini C, Avino R (2012) High-resolution shallow seismic tomography of a hydrothermal area: application to the Solfatara, Pozzuoli. Geophys J Int 189:1725-1733. doi:10.1111/j.1365-246X.2012.05451.x

Li Y, Oldenburg DW (1992) Approximate inverse mappings in DC resistivity problems. Geophys J Int 109:343-362. doi:10.1111/j.1365-246X.1992.tb00101.x

Loke MH, Barker RD (1995) Least-squares deconvolution of apparent resistivity pseudosections. Geophysics 60:1682–1690. doi:10.1190/1.1443900

Loke MH, Barker RD (1996) Rapid least-squares inversion of apparent resistivity pseudosections by a quasi-Newton method. Geophys Prospect 44:131-152. doi:10.1111/j.1365-2478.1996.tb00142.x

Loke MH (2014) Tutorial: 2-D and 3-D electrical imaging surveys. Geotomo Softwares, Penang. www.geotomosoft.com

Mauriello P, Patella D (1999) Resistivity anomaly imaging by probability tomography. Geophys Prospect 47:411-429. doi:10.1046/j.1365-2478.1999.00137.x

Mauriello P, Patella D (2001) Localization of maximum-depth gravity anomaly sources by a distribution of equivalent point masses. Geophysics 66:1431-1437. doi:10.1190/1.1487088

Mauriello P, Patella D (2008a) Geoelectrical anomalies imaged by polar and dipolar probability tomography. Prog Electromagnet Res 87:63-88. doi:10.2528/PIER08092201

Mauriello P, Patella D (2008b) Integration of geophysical datasets by a conjoint probability tomography approach. Application to Italian active volcanic areas. Ann Geophys 51:167-180. doi:10.4401/ag-3042

Mauriello P, Patella D (2009) A data-adaptive probability-based fast ERT inversion method. Prog Electromagnet Res 97:275-290. doi:10.2528/PIER09092307

Mauriello P, Patella D, Petrillo Z, Siniscalchi A, Iuliano T, Del Negro C (2004) A geophysical study of the Mount Etna volcanic area. In: Bonaccorso A, Calvari S, Coltelli M, Del Negro C, Falsaperla S (eds) Mt.Etna: Volcano Laboratory. Geophysical Monograph Series 143 AGU, pp 273-291. ISBN:9780875904085

Nettleton LL (1971) Elementary Gravity and Magnetics for Geologists and Seismologists. Monograph Series 1 SEG, Tulsa

Nettleton LL (1976) Gravity and Magnetics in Oil Prospecting. McGraw-Hill, New York. ISBN:9780070463035

Oliveri del Castillo A, Palumbo A, Percolo E (1968) Contributo allo studio della Solfatara di Pozzuoli (Campi Flegrei) mediante osservazione gravimetriche. Annali Osservatorio Vesuviano 22:217-225

Ortega AI, Benito-Calvo A, Porres J, Pérez-González A, Martín Merino,MA (2010) Applying electrical resistivity tomography to the identification of endokarstic geometries in the Pleistocene sites of the Sierra de Atapuerca (Burgos, Spain). Archaeol Prosp 17:233-245. doi:10.1002/arp.392

Park SK, Van G (1991) Inversion of pole-pole data for 3D resistivity structure beneath arrays of electrodes. Geophysics 56:951-960. doi:10.1190/1.1443128

Patella D (1997a) Introduction to ground surface self-potential tomography. Geophys Prospect 45:653-681. doi:10.1046/j.1365-2478.1997.430277.x

Patella D (1997b) Self-potential global tomography including topographic effects. Geophys Prospect 45:843-863. doi:10.1046/j.1365-2478.1997.570296.x

Petrosino S, Damiano N, Cusano P, Di Vito MA, de Vita S, Del Pezzo E (2012) Subsurface structure of the Solfatara volcano (Campi Flegrei caldera, Italy) as deduced from joint seismic-noise array, volcanological and morphostructural analysis. Geochem Geophys Geosys 13(7):1-25. doi:10.1029/2011GC004030

Richards K, Revil A, Jardani A, Henderson F, Batzle M, Haas A (2010) Pattern of shallow ground water flow at Mount Princeton Hot Springs, Colorado, using geoelectrical methods. J Volzanol Geoth Res 198:217-232. doi:10.1016/j.jvolgeores.2010.09.001

Rosi M, Sbrana A (1987) Introduction, geological setting of the area, stratigraphy, description of mapped products, petrography, tectonics In: Rosi M, Sbrana A (eds) Phlegrean Fields. QRS 114(9) CNR, Rome, pp 9-93. ISBN:451

Sasaki Y (1994) 3D resistivity inversion using the finite-element method. Geophysics 59:1839-1848. doi:10.1190/1.1443571

Shima H (1990) Two-dimensional automatic resistivity inversion technique using alpha centers, Geophysics 55:682-694. doi:10.1190/1.1442880

Skeels DC (1963) An approximate solution of the problem of maximum depth in gravity interpretation. Geophysics 28:724-735. doi:10.1190/1.1439262

Soupios PM, Vallianatos F, Papadopoulos I, Makris JP, Marinakis M (2005) Surface-geophysical investigation of a landfill in Hania, Crete. In: Agiountantis Z, Komnitsas K (eds) International Workshop Geoenv 2005. Heliotopos Conferences, Athens, pp 149-156. ISBN:960-881-53-7-1

Soupios PM, Papadopoulos I, Kouli M, Georgaki I, Vallianatos F, Kokkinou E (2007) Investigation of waste disposal areas using electrical methods: a case study from Chania, Crete, Greece. Environ Geol 51:1249-1261. doi:0.1007/s00254-006-0418-7

Todesco M, Chiodini G, Macedonio G (2003) Monitoring and modelling hydrothermal fluid emission at La Solfatara (Phlegraean Fields, Italy). An interdisciplinary approach to the study of diffuse degassing. J Volcanol Geoth Res 125:57-79. doi:10.1016/S0377-0273(03)00089-1

Todesco M, Berrino G (2005) Modelling hydrothermal fluid circulation and gravity signals at the Phlegrean Fields caldera. Earth Planet Sci Lett 240:328–338. doi:10.1016/j.epsl.2005.09.016

Tripp AC, Hohmann GW, Swift CM (1984) Two-dimensional resistivity inversion. Geophysics 49:1708-1717. doi:10.1190/1.1441578

Troiano A, Petrillo Z, Di Giuseppe MG, Balasco M, Diaferia I, Di Fiore B, Siniscalchi A, Patella D (2008) About the shallow resistivity structure of Vesuvius volcano. Ann Geophys 51:181-189. doi:10.4401/ag-3043

Troiano A, Di Giuseppe MG, Petrillo Z, Troise C, De Natale G (2011) Ground deformation at calderas driven by fluid injection: modelling unrest episodes at Campi Flegrei (Italy). Geophys J Int 187:833-847. doi:10.1111/j.1365-246X.2011.05149.x

Troiano A, Di Giuseppe MG, Patella D, Troise C, De Natale G (2014) Electromagnetic outline of the Solfatara-Pisciarelli hydrothermal system, Campi Flegrei (Southern Italy). J Volcanol Geoth Res 277:9-21. doi:10.1016/j.jvolgeores.2014.03.005

Van Zijl JSV (1985) A practical manual on the resistivity method. Geophysics Division Nat. Phys. Res. Lab., Counc. Sci. Ind. Res., South Africa

Vargemezis G (2014) 3D geoelectrical model of geothermal spring mechanism derived from VLF measurements: A case study from Aggistro (Northern Greece). Geothermics 51:1-8. doi:10.1016/j.geothermics.2013.09.001

Ward SH (1990) Resistivity and induced polarization methods. In: Ward SH (ed) Geotechnical and Environmental Geophysics, Vol.I: Review and Tutorials. Investigations in Geophysics 5 SEG, Tulsa, pp 147-189. ISBN:978-0-931830-99-0

Wardman JB, Wilson TM, Bodger PS, Cole JW, Johnston DM (2012) Investigating the electrical conductivity of volcanic ash and its effect on HV power systems. Phys Chem Earth A 45-46: 128-145. doi:10.1016/j.pce.2011.09.003

Xia J, Ludvigson G, Miller RD, Mayer L, Haj A (2010) Delineation of a volcanic ash body using electrical resistivity profiling. J Geophys Eng 7:267–276. doi:10.1088/1742-2132/7/3/005

Zeyen H, Pessel M, Ledésert B, Hébert R, Bartier D, Sabin M, Lallemant S (2011) 3D electrical resistivity imaging of the near-surface structure of mud-volcano vents. Tectonophysics 509:181-190. doi:10.1016/j.tecto.2011.05.007

1 **FIGURE CAPTIONS**
2
3 **Fig. 1** Digital elevation map of the Campi Flegrei composite caldera (Southern Italy). The
4 red box includes the Solfatara crater, where the ERT survey was carried out.
5
6 **Fig. 2** Aerial photo of the Solfatara crater. The white area is the vegetation-free degassing
7 area. The black diamonds labelled BG, BN, LS and LF indicate the *Bocca Grande* (Big vent),
8 *Bocca Nuova* (New vent), *Le Stufe* (Stoves) and *La Fangaia* (Mud pool) main fumarole fields,
9 respectively, in the crater. The yellow lines numbered from 1 to 8 indicate the new ERT
10 profiles. The cyan dashed line indicates the western half of the CSAMT-MT profile discussed
11 in Troiano et al. (2014).
12
13 **Fig. 3a** Apparent resistivity pseudosections across the profiles ERT1, ERT2, ERT4, ERT5,
14 ERT6 and ERT7 reported in Fig.2.
15
16 **Fig. 3b** Apparent resistivity pseudosections across the profile ERT3 and ERT8 reported in
17 Fig.2.
18
19 **Fig. 4** Horizontal slices of the near-surface resistivity pattern beneath the Solfatara crater at
20 six different depths, constructing using the 3D PERTI algorithm. The vertical level of the
21 slices is given as depth below ground level, taking an *x,y* reference plane coincident with the
22 flat central area of the crater, placed at 93 m asl, and (in parentheses) directly as height above
23 sea level. For clarity, the ERT profiles in fig.2 are drawn with dashed lines in the top slice.
24 Along the colour scale the subdivision in low, intermediate and high resistivity classes, LR, IR
25 and HR, respectively, is reported.
26
27 **Fig. 5** Horizontal slices of the near-surface resistivity pattern beneath the Solfatara crater at
28 six different depths, deduced by interpolating the model data obtained along each individual
29 profile by applying the RES2DINV algorithm. The style used to represent the maps is the
30 same as in Fig.5.
31
32 **Fig. 6** Horizontal slices at increasing pseudodepth, showing the pattern of the modulus of the
33 discrepancy index, calculated as the difference between the field and simulated apparent
34 resistivity values, divided by the simulated apparent resistivity. In the slices, *z* stands for
35 pseudodepth, unlike in maps of Fig.4 and Fig.5, where it is depth. The field apparent
36 resistivity dataset includes the measured apparent resistivity values and those extrapolated
37 from them in all of the points not sensed by the ERT array, down to the maximum
38 pseudodepth of 80 m. The simulated apparent resistivity dataset has been derived from the
39 PERTI model depicted in Fig.4.
40
41 **Fig. 7** 3D perspective, viewed vertically upward, of the link between the CSAMT-MT depth
42 section obtained by Troiano et al. (2014) with 80 mbgl slice extracted from the 3D ERT model
43 (Fig. 5f) presented in this paper. The line of intersection of the two cross sections corresponds
44 with the trace of the CSAMT-MT profile, drawn with a cyan dashed line in Fig.2.
45
46 **Fig. 8** CO_2 flux, soil temperature and Bouguer anomaly contour lines superimposed onto a
47 synthetic 3D version of the PERTI model. The bluish and reddish volumes represent the LR
48 ($\rho \leq 4$ Ωm) and HR ($\rho \geq 60$ Ωm) resistivity classes, respectively. The white area includes the
49 whole IR class (5 Ωm $\leq \rho \leq 50$ Ωm).
50
51 **Fig. 9** Estimation of the depth to the centres of the sources of the two gravity lows appearing
52 in the Bouguer map within the Solfatara crater, under the simplifying assumption that the

1   causative bodies have spherical symmetry. The two radial lines A-A' and B-B' have been
2   selected through the centres of the minima, nearly along the trend direction of the field
3   (regional gravity). Nettleton's approximate approach (Nettleton 1971) has been used,
4   consisting of: (1) tracing the estimated trend profile, which has been assumed to be linear (red
5   straight-line in both the bottom diagrams); (2) plotting the gravity anomaly values (green full
6   circlets) extracted from the Bouguer contour drawing (top map); (3) plotting the residual
7   gravity anomaly values (blue full circlets) using the trend line as zero level; (4) computing and
8   drawing, by trial-and-error, the synthetic sphere effect curve (red full ellipses) matching the
9   gravity residual plots; (5) finding the horizontal distance $2x_{1/2}$ between the symmetrical points
10   where the residual anomaly is half the value at its centre.

Figure 1
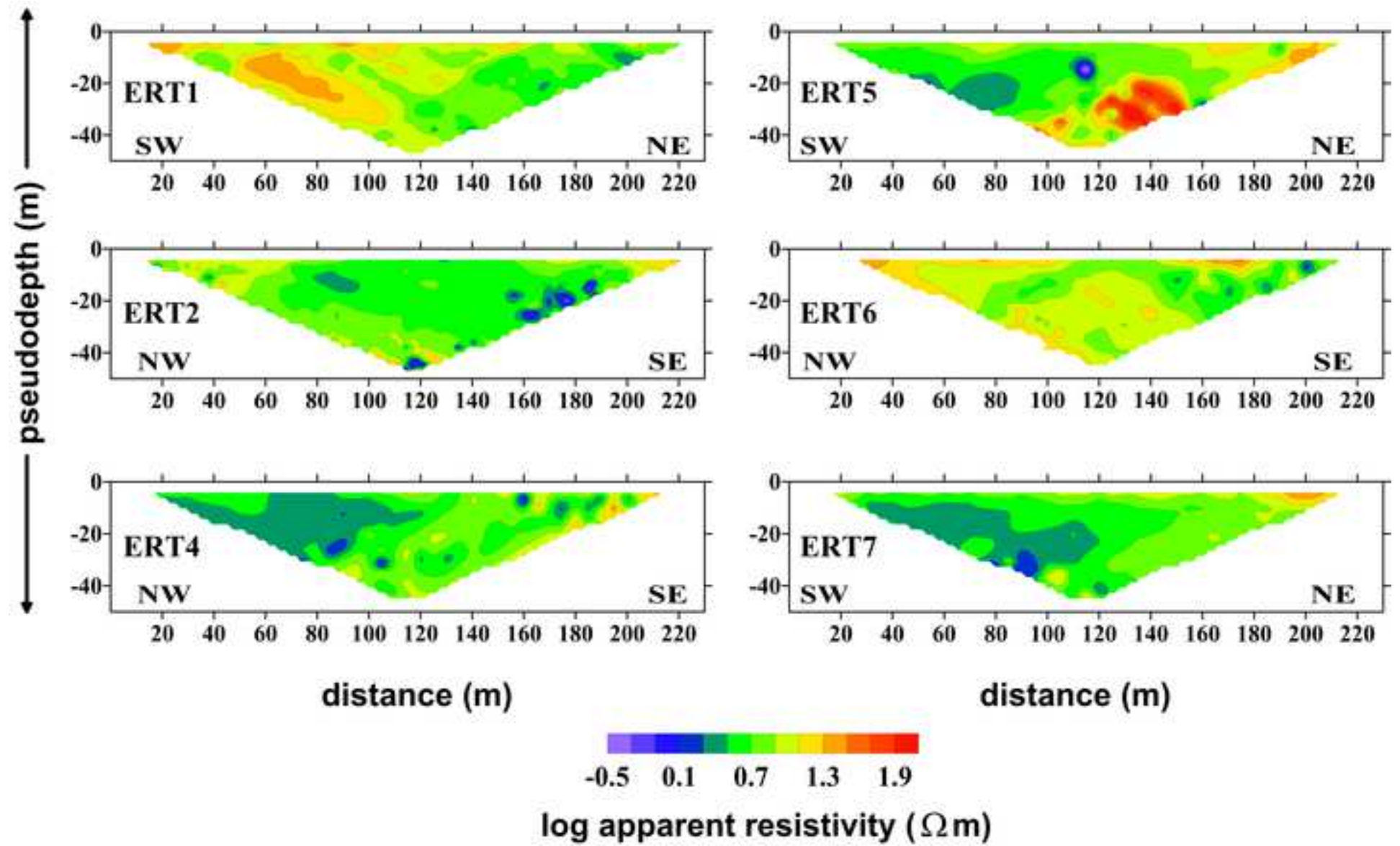Click here to download high resolution image
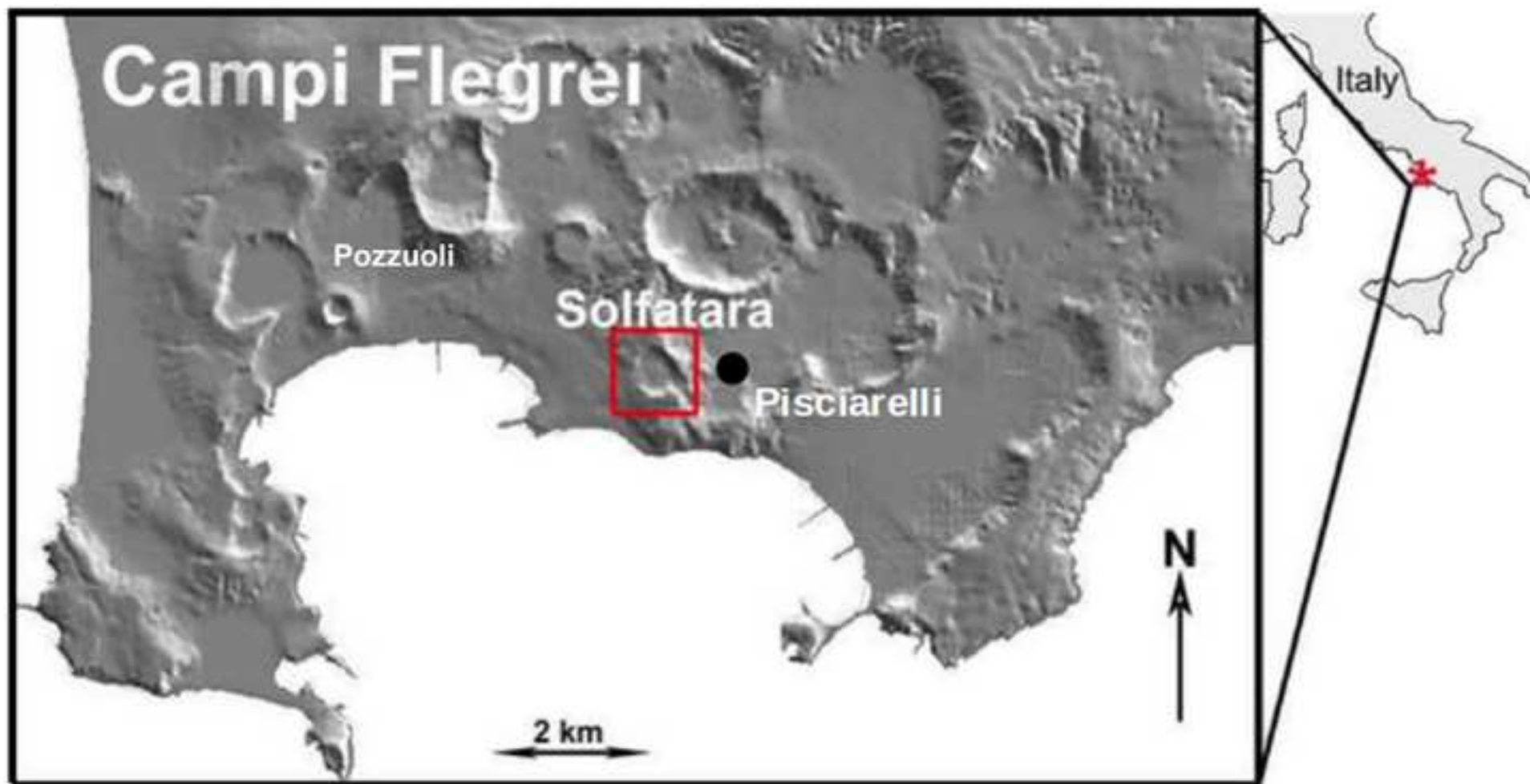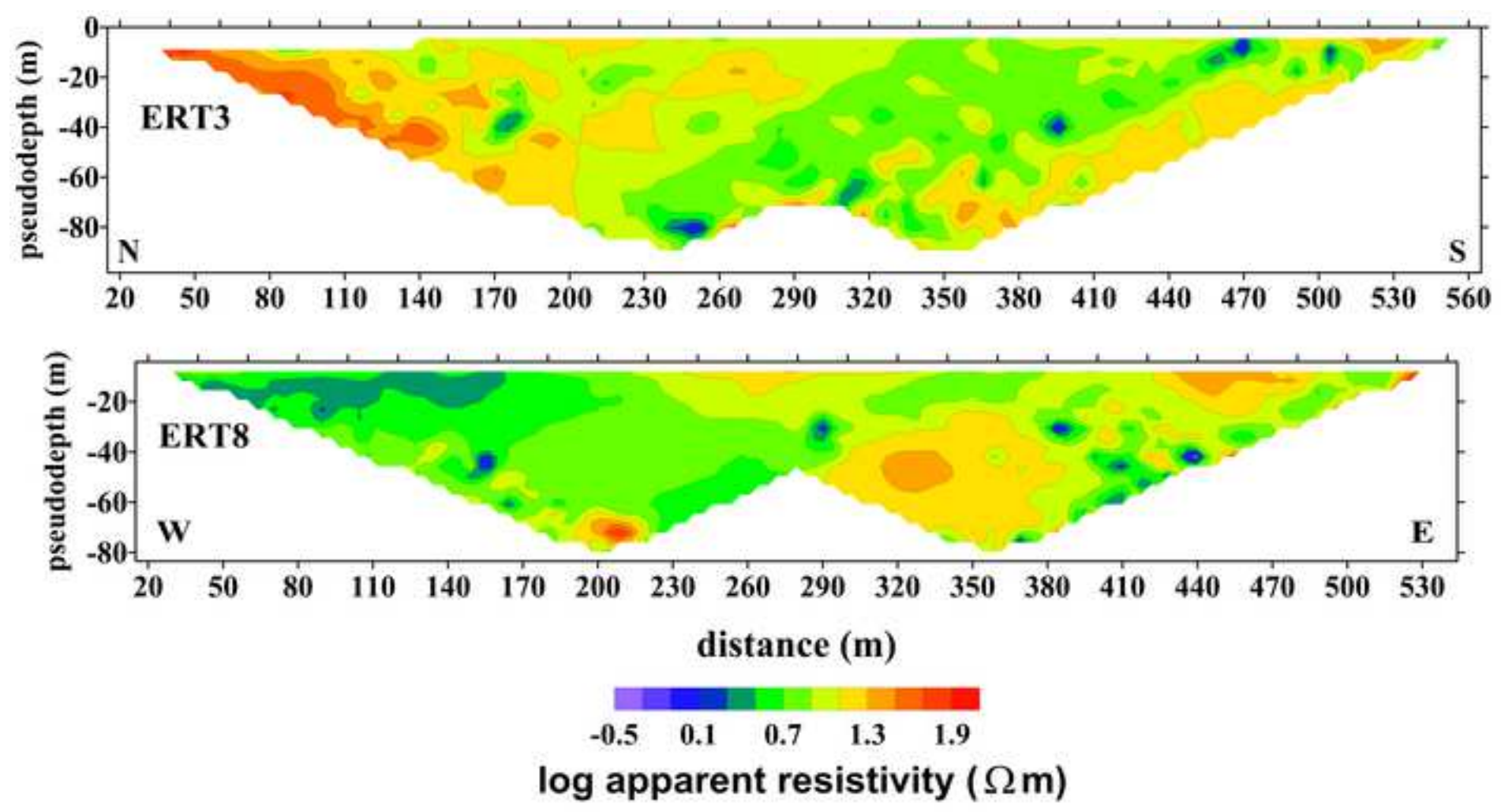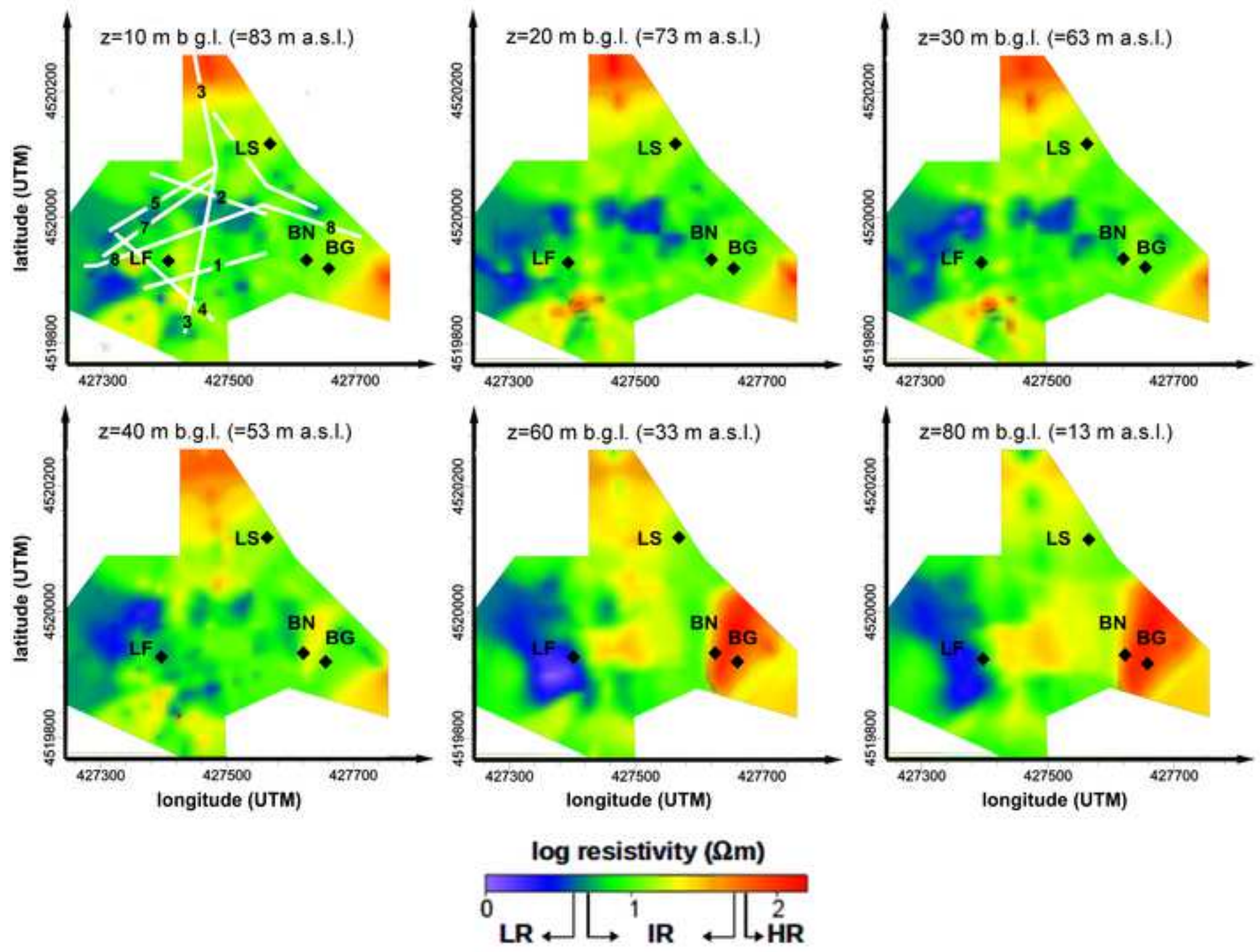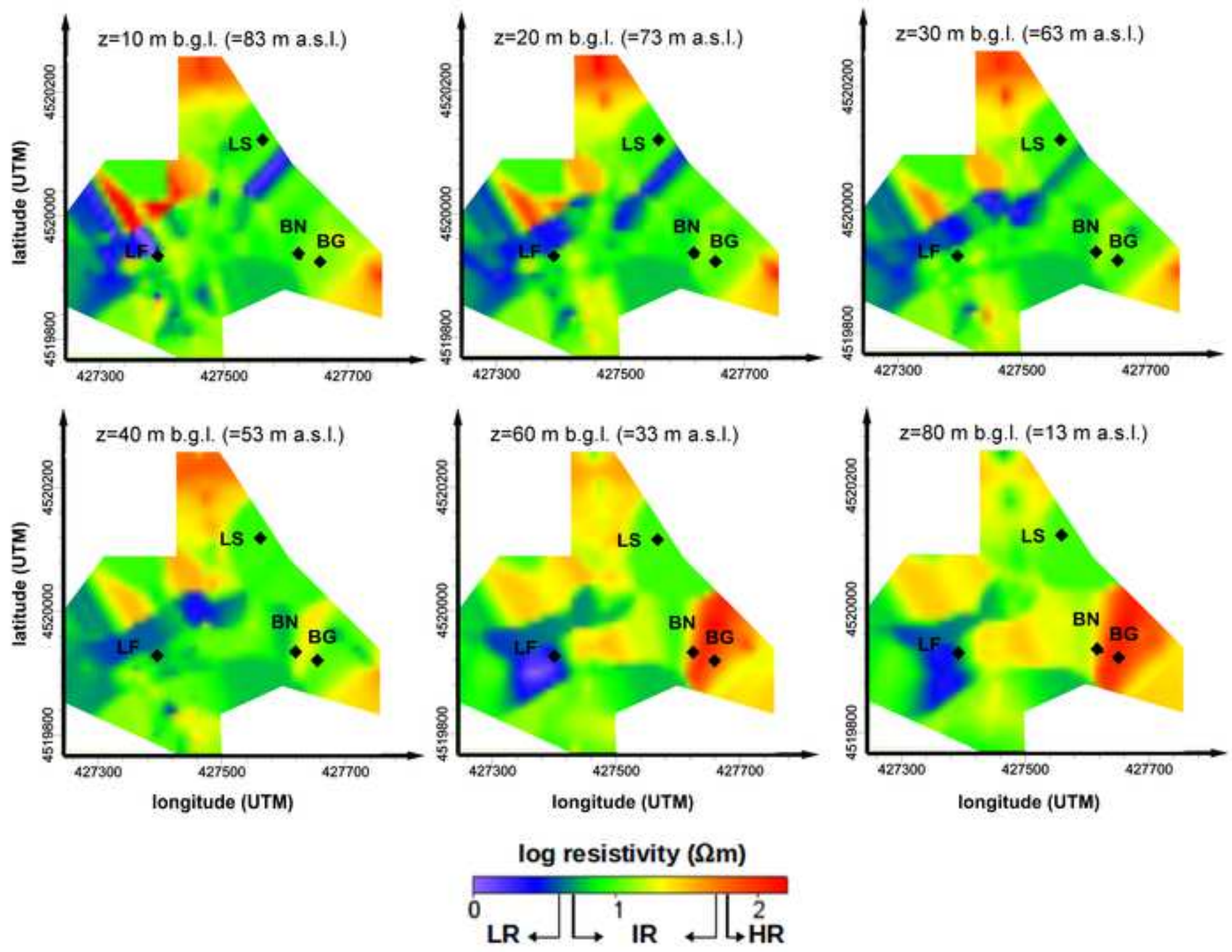
distance (m)

log apparent resistivity (Ωm)
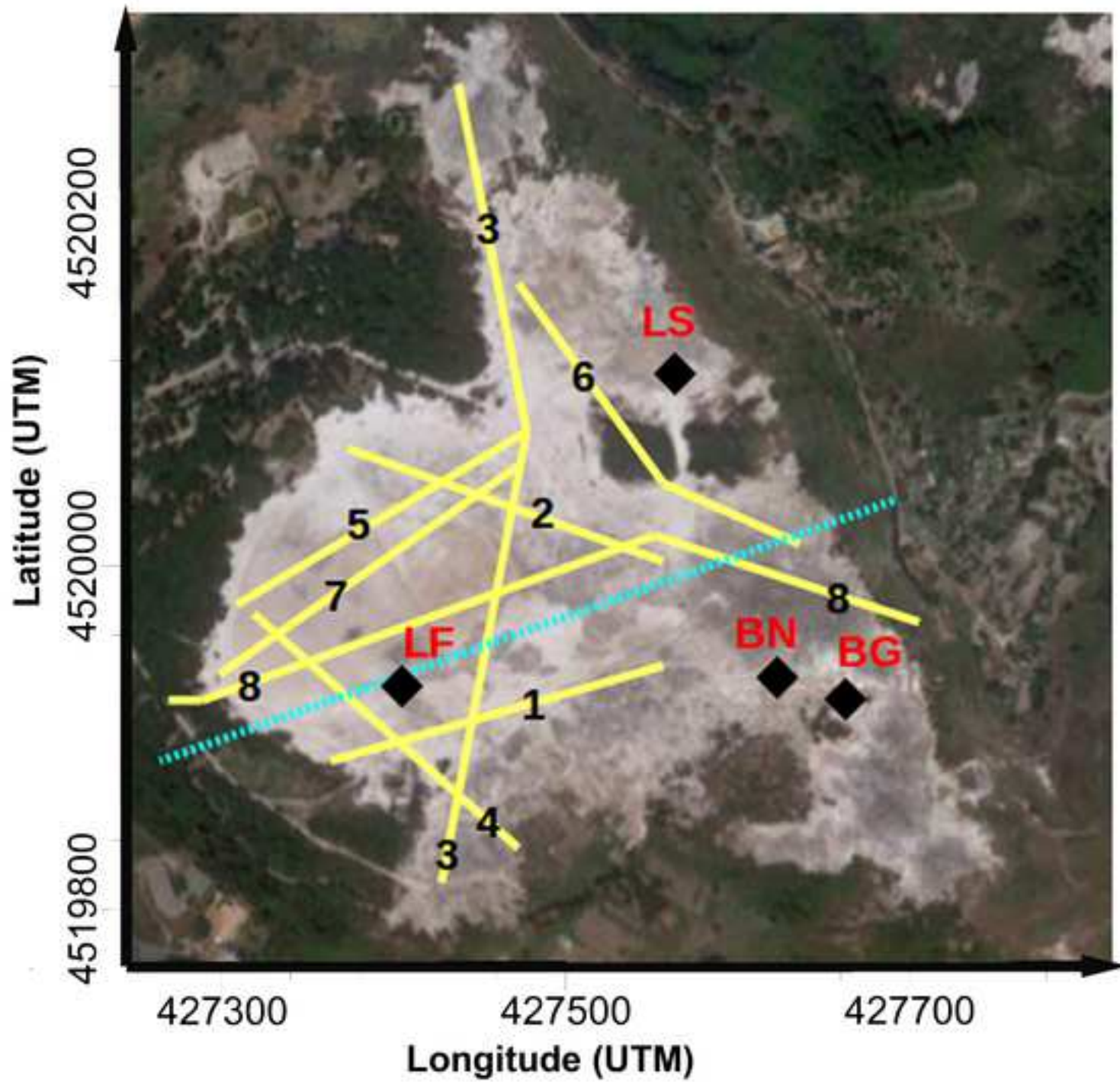
Figure 4
Click here to download high resolution image

Figure 5
Click here to download high resolution image
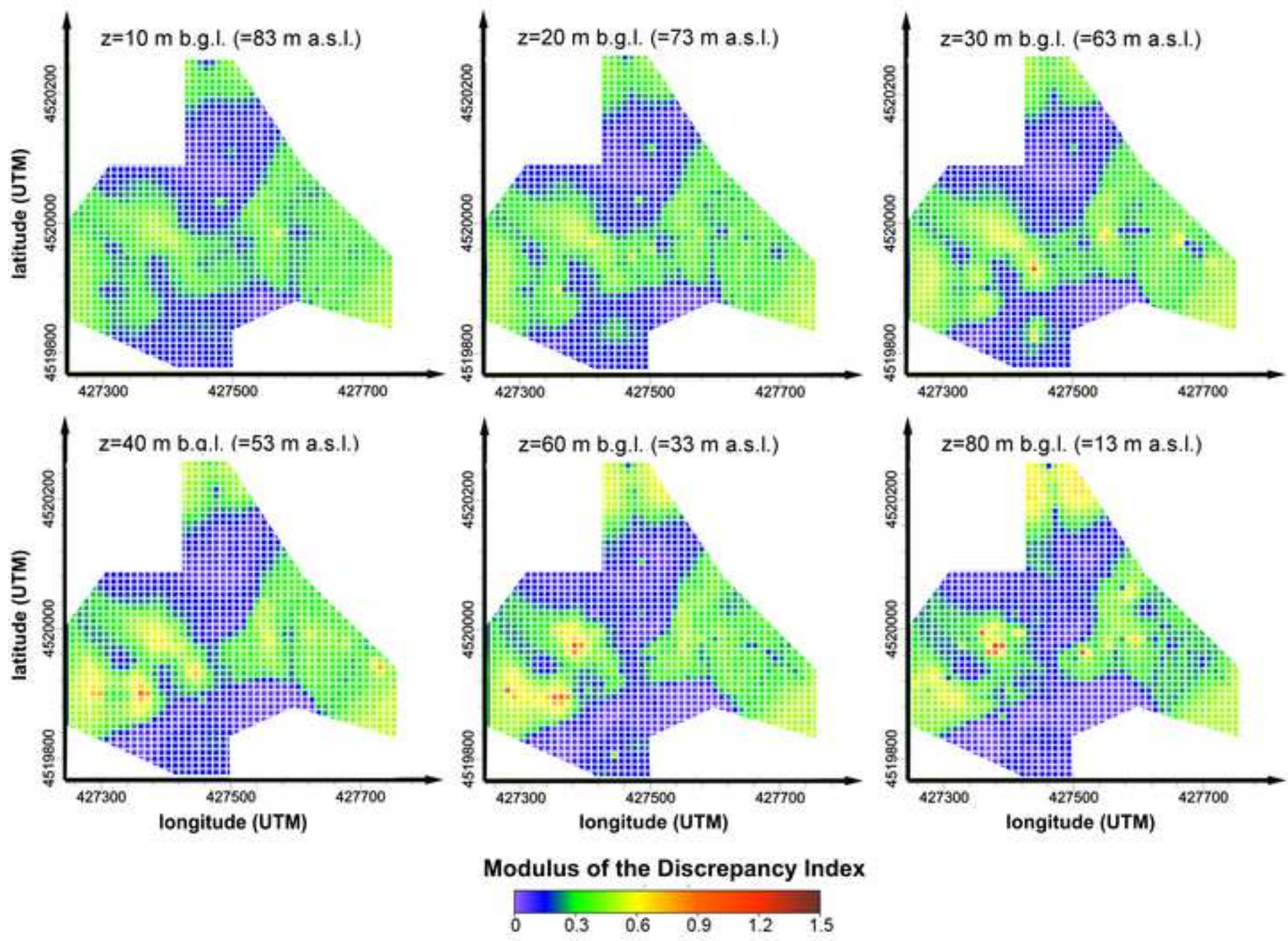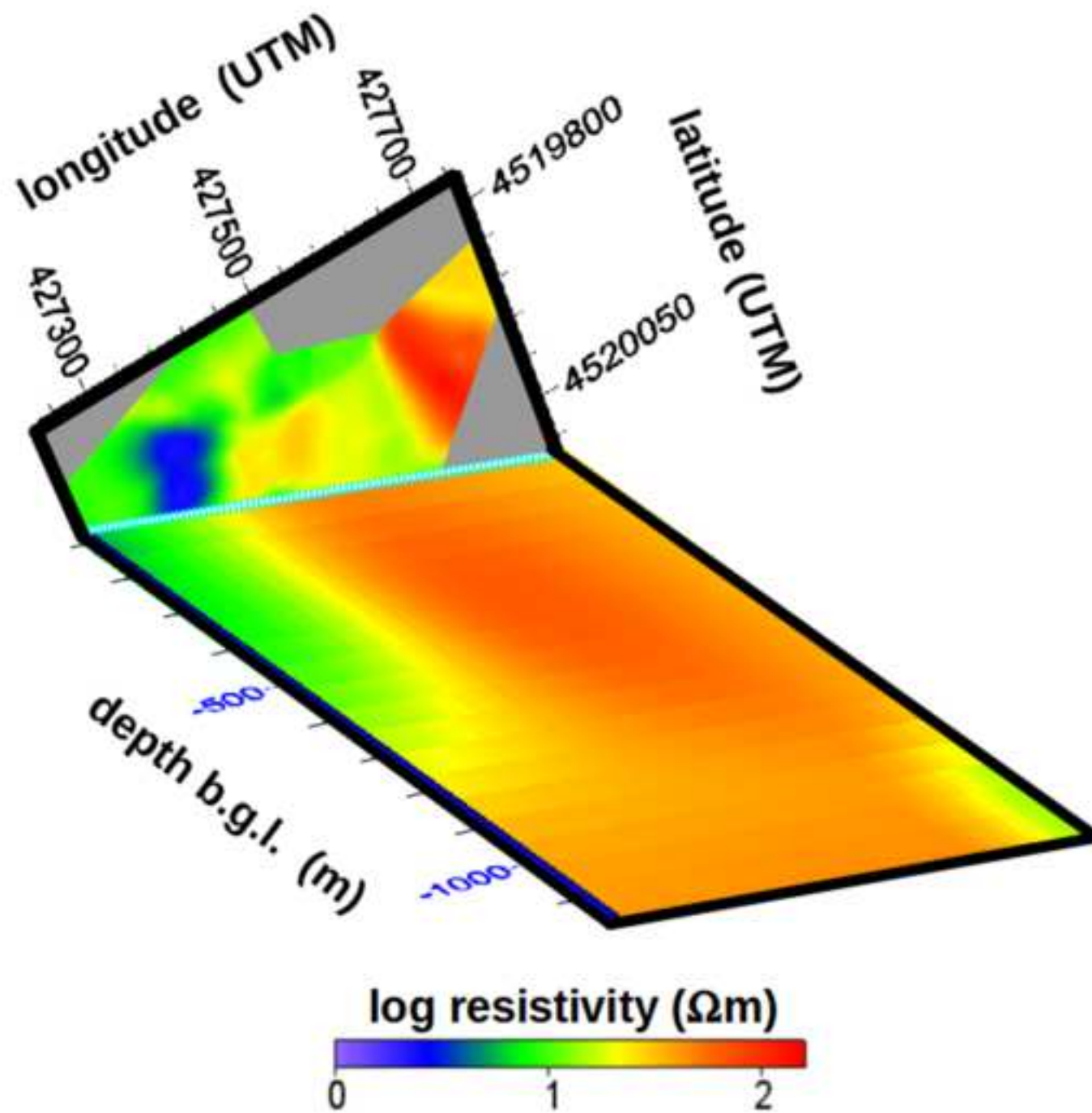
Figure 6
Click here to download high resolution image

z=10 m b.g.l. (=83 m a.s.l.)

z=20 m b.g.l. (=73 m a.s.l.)

z=30 m b.g.l. (=63 m a.s.l.)

z=40 m b.g.l. (=53 m a.s.l.)

z=60 m b.g.l. (=33 m a.s.l.)

z=80 m b.g.l. (=13 m a.s.l.)

latitude (UTM)

longitude (UTM)

Modulus of the Discrepancy Index

0   0.3   0.6   0.9   1.2   1.5

CO$_2$ flux (g m^{-1}day^{-1} x10^4)

0   0.77   1.54   2.31   3.08

soil temperature (°C)

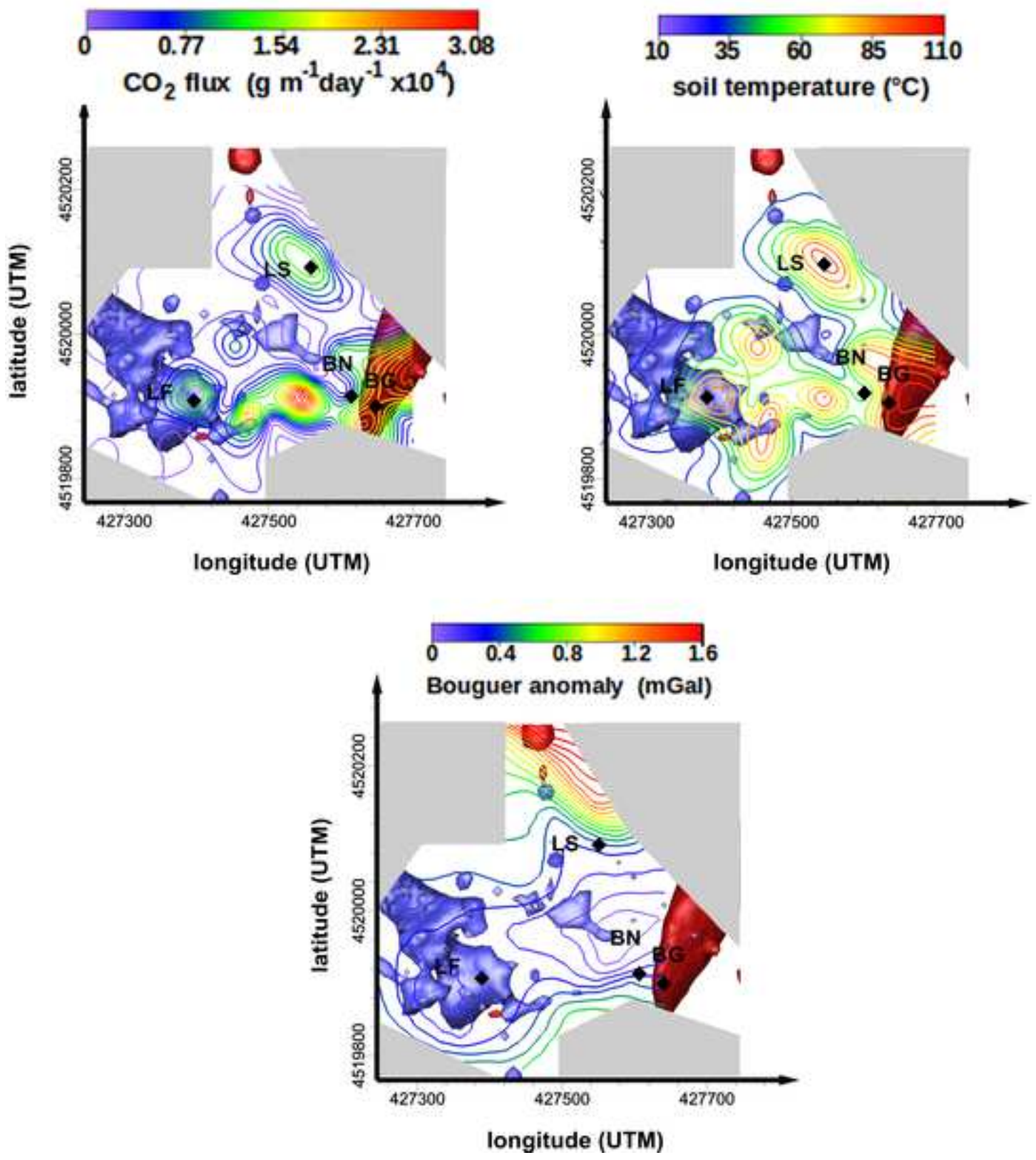10   35   60   85   110

Bouguer anomaly (mGal)

0   0.4   0.8   1.2   1.6

Figure 9
Click here to download high resolution image